J. Fluid Mech. (2004), *vol.* 520, *pp.* 267–295. © 2004 Cambridge University Press
DOI: 10.1017/S0022112004001612 Printed in the United Kingdom

Interaction of a deep-water wave with a vertical cylinder: flow structure and loading

By Y. YANG AND D. ROCKWELL

Department of Mechanical Engineering and Mechanics, 354 Packard Laboratory, 19 Memorial Drive West, Lehigh University, Bethlehem, PA 18015, USA
dor0@lehigh.edu

(Received 20 February 2004 and in revised form 5 August 2004)

Interaction of a deep-water wave with a vertical cylinder is characterized using techniques of high-image-density particle image velocimetry, in conjunction with measurement of the transverse and in-line loading coefficients. Phase-locked patterns of locally two-dimensional vortex formation are attainable only for sufficiently high values of the Keulegan–Carpenter number KC, e.g. $KC \geqslant 12$. Even in these cases, such patterns are interrupted by non-phase-locked patterns that, nevertheless, show basic forms, including mode inversion or switching of the initially formed vortex from the cylinder, along with patterns of symmetrical vortex formation, all represented by patterns of instantaneous vorticity.

Three-dimensionality of the flow structure along the span of the cylinder shows, at relatively low KC, patterns of transverse velocity v and streamwise vorticity ω_x that have well-defined spanwise spacing. This spacing decreases in a continuous fashion with depth beneath the free surface, and is in accord with the decrease of local KC with depth, i.e. decrease of the diameter of the local particle trajectory. Such three-dimensional patterns are, however, not phase repetitive over a large number of wave cycles.

At sufficiently high values of KC, it is possible to identify basic classes of three-dimensional patterns. When regions of transverse velocity show like sign over a significant spanwise extent of the cylinder, the transverse loading coefficient is relatively large. As the number of zero crossings between the positive and negative regions of v increases, the transverse loading coefficient decreases accordingly. Generally speaking, at these higher values of KC, patterns of streamwise vorticity are much less ordered, and of smaller scale; they are embedded within larger-scale well-defined patterns of the transverse velocity v along the span.

Taken together, the patterns of locally two-dimensional (sectional) structure and the three-dimensional structure along the span indicate a criterion for locally phase-locked quasi-two-dimensional vortex formation: it occurs when the pattern of transverse velocity is of the same sign over a significant spanwise distance along the span of the cylinder.

1. Introduction

Cables, risers and other configurations are subjected to unsteady wave motion in the ocean environment, which can lead to unsteady loading and vibration. In recent decades, much effort has been devoted to investigations of wave–structure interactions. The following summaries provide brief synopses of these advances.

https://doi.org/10.1017/S0022112004001612 Published online by Cambridge University Press

1.1. *Flow structure due to planar oscillations of a cylinder or flow*

If the wave has a wavelength that is very long, then the essential features of the wave–cylinder interaction can be simulated with planar oscillations of the cylinder in quiescent fluid or, equivalently, planar oscillatory flow past a stationary cylinder. Irrespective of the approach, the primary physical parameters are the Keulegan–Carpenter number $KC = 2\pi A_0/D$, in which A_0 is the displacement amplitude of either the oscillatory flow or the cylinder motion and D is the diameter of the cylinder. In addition, one must consider the Stokes number, $\beta = fD^2/\nu$, where f is the frequency of the motion and ν is the kinematic viscosity. In recent decades, substantial advances have been made in our understanding of patterns of vortex formation, as well as the in-line and transverse forces on the cylinder. Investigations that address one or more of these features include Singh (1979), Bearman *et al.* (1981), Sarpkaya & Isaacson (1981), Ikeda & Yamamoto (1981), Iwagaki, Asano & Nagai (1983), Williamson (1985), Obasaju, Bearman & Graham (1988), Dütsch *et al.* (1998*a*) and Lin & Rockwell (1999).

Even for these simple scenarios of planar motion, significant departures from two-dimensionality may occur. One indicator of the spanwise three-dimensionality is the spanwise correlation coefficient of the fluctuating surface pressure. Such correlations were measured by Obasaju *et al.* (1988) and Kozakiewicz, Sumer & Fredsøe (1992). In addition, the sectional qualitative visualization of Obasaju *et al.* (1988) revealed that the process of vortex formation on two different spanwise planes was not in phase, which indicates the existence of three-dimensional mechanism.

Qualitative visualization along the span of the cylinder, performed by Honji (1981), revealed ordered three-dimensional modes that had a spanwise wavelength λ, normalized with respect to the cylinder diameter D, of the order of $\lambda/D = 0.5$ to 1.0; these experiments involved planar oscillation of the cylinder in quiescent water. Sarpkaya (1986, 2002) further pursued this type of Honji instability, with emphasis on its inception, in conjunction with the onset of separation and turbulence on the oscillating cylinder. Tatsuno & Bearman (1990) extensively characterized the possible types of three-dimensionality over ranges of Keulegan–Carpenter number KC and Stokes number β. A number of regimes were identified with spanwise wavelengths from $\lambda/D = 0.8$ to 6.0. Numerical simulation of these types of three-dimensional modes was performed by Dütsch, Durst & Brenner (1998*b*) and Dütsch (2000). Their simulations, which were performed at relatively low values of KC and Reynolds number Re, showed spanwise structure having a wavelength $\lambda/D = 2.5$. Elston, Blackburn & Sheridan (2000) undertook a direct numerical simulation in conjunction with a Floquet analysis to characterize the three-dimensional modes as a function of KC and β. They showed that the spanwise patterns involved ordered concentrations of vorticity of wavelengths $\lambda/D = 1.4$ to 3.9.

1.2. *Loading coefficients of a vertical cylinder in a wave*

Interaction of a free-surface wave with a cylinder has focused almost entirely on the loading coefficients of the cylinder. This loading has been defined by Ramberg & Niedzwecki (1979), Chakrabarti (1980), Stansby, Bullock & Short (1983), Bearman, *et al.* (1985) and Tørum (1989). Furthermore, simulation of the wave motion by Sarpkaya (1984), which involved vertical oscillations of the cylinder in a planar oscillatory flow, also yielded values of loading coefficients. Determination of the loading is often done in a field environment, and a representative investigation using this approach is Dean, Dalrymple & Hudspeth (1981). Sumer & Fredsøe (1997)

https://doi.org/10.1017/S0022112004001612 Published online by Cambridge University Press

provide a comprehensive assessment of the loading arising from wave–vertical cylinder interaction, relative to the corresponding loading due to planar oscillatory flow.

1.3. *Wave–vertical cylinder interaction*

Very little effort has been devoted to characterization of the quasi-two-dimensional (sectional) vortex patterns, or to the spanwise three-dimensionality arising from the interaction of a wave with a vertical cylinder. Kaye (1989) employed qualitative particle visualization at the free surface of a wave interacting with a vertical cylinder in order to determine the overall patterns of vortex formation. Yang & Rockwell (2002) employed quantitative imaging for the case of an intermediate wave–cylinder interaction, whereby the oscillatory motion was predominantly in the horizontal direction over the entire depth of the wave tank. For such an intermediate wave, elongated elliptical particle motion occurs in the region immediately beneath the free surface, which transforms to planar oscillatory flow as the bottom of the wave tank is approached. Possible modes of quasi-two-dimensional (sectional) vortex formation were not characterized in terms of patterns of vorticity and streamline topology, which is one of the goals of the present investigation. Regarding three-dimensionality, the total height H of the submerged portion of the cylinder was large compared to its diameter, i.e. $H/D = 55$, and it was therefore possible to generate various types of three-dimensional modes having long spanwise wavelengths, e.g. on the order of $10D$. Embedded within these long-wavelength modes were streamwise concentrations of vorticity ω_x with spacings in the range of $\lambda/D = 1$ to 4.

For the case of a deep-water wave, the wake structure from the cylinder is expected to exhibit even more complex three-dimensional modes along its span. For a given cross-section of the near wake, which indirectly accounts for the existence of spanwise three-dimensionality, Sirisup *et al.* (2004) describe a low-order simulation of the flow patterns. This simulation is driven by experimental quantitative imaging of the wake patterns. For very low values of KC, Ozgoren & Rockwell (2004) describe transformations between phase-locked and non-phase-locked modes of sectional vortex formation for stationary and oscillating cylinders in a deep-water wave.

The focus of the present investigation is on the interaction of a deep-water wave with a vertical cylinder, with emphasis on representations of both the quasi-two-dimensional (sectional) and three-dimensional flow physics. The distinctively different characteristics of a deep wave, relative to shallow and intermediate waves, leads to the definition of a number of issues, which are addressed in the following.

1.4. *Overview of unresolved issues*

The foregoing investigations have provided considerable insight and serve as a basis for characterization of the flow structure due to interaction of a deep-water wave with a vertical cylinder. A deep-water wave involves particle trajectories having a circular form, whose amplitude decreases exponentially with depth. Furthermore, the axes of these particle trajectories are orthogonal to the axis of the cylinder. One therefore expects distinctive patterns of vortex formation in relation to the loading on the cylinder. In essence, the major points, which to date have remained unclarified, are as follows:

(i) The quasi-two-dimensional (sectional) structure of the wave-induced vortices has not been addressed in relation to patterns of vortex formation arising from planar oscillations of the flow or cylinder. Furthermore, for such planar oscillations, it is possible to attain consistent patterns of vortex formation over a large number of oscillation cycles, i.e. phase locking of the shed vortices to the flow or body motion. The degree

https://doi.org/10.1017/S0022112004001612 Published online by Cambridge University Press

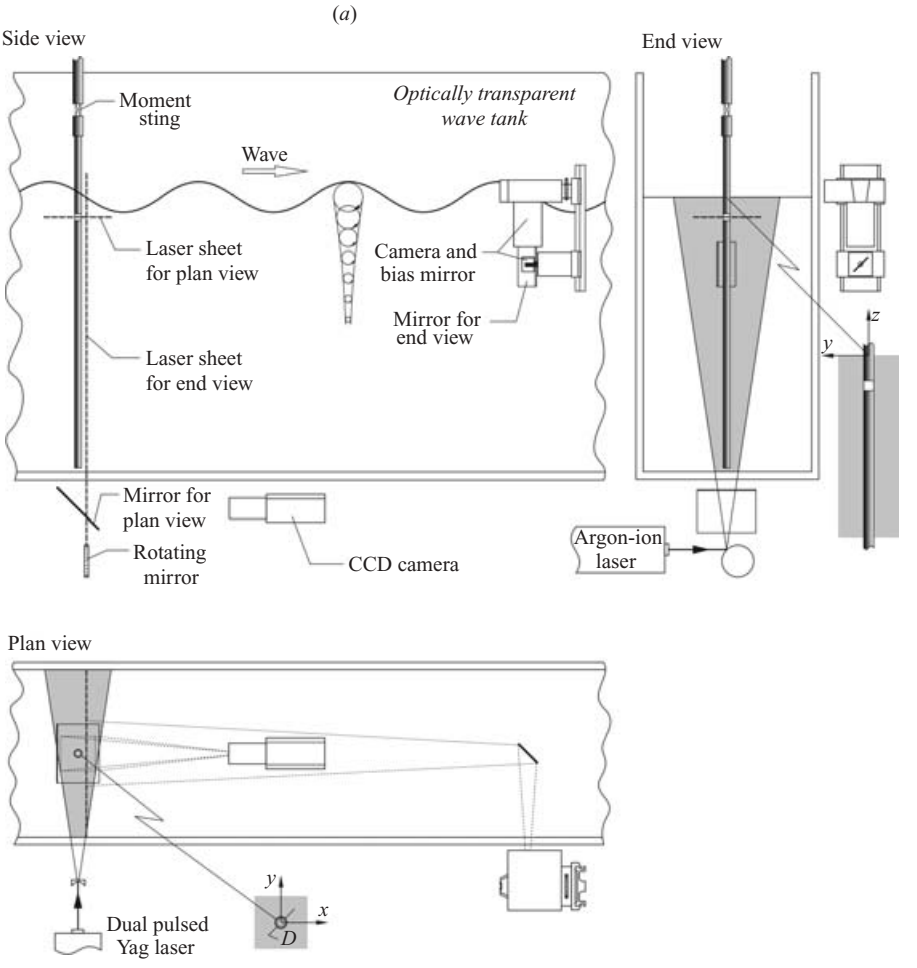


FIGURE 1(*a*). For caption see facing page.

to which phase locking occurs, if at all, has not been pursued for vortex shedding in a deep-water wave. When phase-locking does not occur, classical phase-averaging of a sequence of instantaneous phase-referenced states of the vortex formation does not provide a valid representation of the actual physics of the vortex patterns.

(ii) The nature of the three-dimensional flow structure along the span of the cylinder in a deep-water wave is expected to be particularly complex, in view of the lack of uniformity of the wave. Even for planar oscillations of the cylinder or flow, well-defined ordered patterns of three-dimensionality along the span of the cylinder occur, as described above. The existence of analogous patterns in presence of a deep-water wave has not been addressed. Moreover, the persistence, i.e. degree of phase-locking over a number of wave cycles of possible spanwise patterns, remains unexplored.

(iii) The instantaneous loading coefficients on the cylinder will be, of course, a function of the aforementioned flow structure. The link has not yet been established between whole-field representations of the quasi-two-dimensional and three-dimensional flow structure and the instantaneous in-line and transverse loading coefficients.

https://doi.org/10.1017/S0022112004001612 Published online by Cambridge University Press

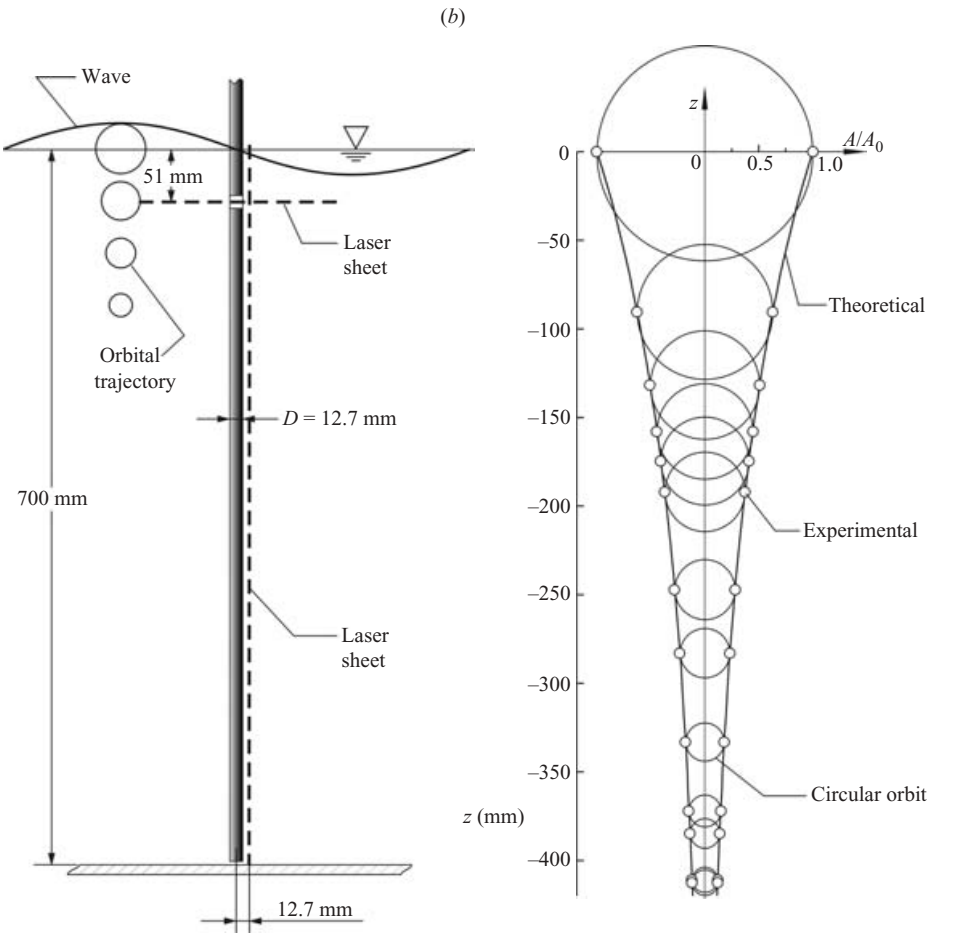


FIGURE 1. (*a*) Schematic of experimental facility for wave–structure interaction showing laser illumination and image acquisition techniques. (*b*) Schematic of wave–cylinder interaction and comparison of experimental and theoretical orbits of the deep-water wave.

The overall objectives of the present investigation aim to address these issues using techniques of high-image-density particle image velocimetry, which allow instantaneous and phase-averaged whole-field patterns of velocity, vorticity and streamline topology. These representations of the flow structure can be interpreted simultaneously with measurements of the cylinder loading.

2. Experimental system and techniques

A wave tank facility, which is designed for three-dimensional optical access, is shown in figure 1(*a*). It is made of high-quality optical glass on its sides and bottom, and allows laser illumination from arbitrary directions and corresponding imaging of the quasi-two- and three-dimensional flow structure. This wave tank has a depth of 1018 mm, a width of 426 mm, and a length of 9300 mm. For all experiments, the water level was maintained at a depth of 700 mm. A paddle-type wave generator with active control involving force feedback (Edinburgh Designs, Ltd.) generated waves of desired frequency and amplitude. An absorbent porous material was deployed at the opposite end of the wave tank. It involved a 1270 mm long wedge (included angle of 19°).

https://doi.org/10.1017/S0022112004001612 Published online by Cambridge University Press

As indicated in figure 1(*a*), a cylinder of diameter $D = 12.7$ mm and length $L = 876$ mm was mounted at the end of a strain gauge sting above the wave tank. For the experiments described herein, deep-water waves of frequency $f = 1.12$ Hz and amplitude $A_0 = 14.1$ to 36.4 mm were employed. Amplitude A_0 is the radius of the orbital particle trajectory of the wave motion at the free surface. These wave amplitudes correspond to values of Keulegan-Carpenter number at the free surface of $KC = 2\pi A_0/D = 7$ to 18. Unless otherwise indicated, the reference value of KC throughout this paper is always evaluated at the free surface. For all experiments, the value of the Stokes number $\beta = fD^2/\nu = 164$, and the maximum Reynolds number $Re = KC\beta = 3000$.

As indicated in figure 1(*b*), the deep-water wave has circular particle trajectories. Theoretical and experimental representations are compared using dimensionless wave amplitude A/A_0, in which A is the radius of the local particle trajectory, versus depth z. The theoretical variation of A/A_0 versus z is

$$\frac{A}{A_0} = \mathrm{e}^{2\pi z/\lambda},$$

where λ is free-surface wavelength; for the present study, $\lambda = 1220$ mm. At each of the indicated depths, a technique of particle imaging, to be described subsequently, led to the trajectory and thereby the experimental value of A/A_0. As shown in figure 1(*b*), the experimental data points are in accord with the theoretical variation.

Quantitative imaging of the flow structure due to the wave–cylinder interaction involves techniques of high-image-density particle image velocimetry. End view imaging, represented schematically at the top of figure 1(*a*), involved generation of a vertical laser sheet which was positioned $1D$ away from the centreline of the cylinder, and across its near wake. This end-view laser sheet was generated by employing a continuous Argon-ion laser (20 W). The laser beam was reflected from a rotating mirror with forty-eight facets. This mirror was located beneath the wave tank. The effective scanning frequency generated by the rotating faceted mirror, ranged from 64 Hz to 250 Hz over the range of $KC = 7$ to 18. The scanning laser sheet illuminated 12 micron metallic-coated particles, which were essentially neutrally buoyant. The particle images were captured on high-resolution 35 mm film using the camera and bias mirror arrangement shown in the schematic at the top of figure 1(*a*). The narrow vertical mirror shown in the plan view of figure 1(*a*) reflected the pattern of particle images in this end view to the 35 mm camera located outside the wave tank. In essence, this approach generates multiply exposed images of each particle on the 35 mm film. For this configuration shown in figure 1(*a*), the magnification was 1:11.27. Since a deep wave induces significant orbital motion only within certain depth beneath free surface, the field of view was focused to the upper portion of the submerged cylinder, i.e. 405.7 mm × 270.5 mm in the plane of the laser sheet, with the top edge slightly above the wave surface. In order to convert the film-recorded pattern of particle images to digital format, the 300 lines mm^{-1} resolution film was digitized at 125 pixels mm^{-1}. Use of a single-frame cross-correlation technique led to the instantaneous velocity field. The corresponding size of the interrogation window was 90 pixels × 90 pixels. In order to satisfy the Nyquist criterion, the interrogation window is overlapped by 50%. The effective grid size of the velocity field was 4.06 mm. Furthermore, to ensure that the criterion of high-image-density was satisfied, each interrogation window contained at least 40 particle images.

For imaging of the quasi-two-dimensional flow structure, in the indicated horizontal plane of figure 1(*a*), a digital technique (DPIV) was employed. Laser illumination was

https://doi.org/10.1017/S0022112004001612 Published online by Cambridge University Press

from a dual-pulsed Yag laser, located exterior to the wave tank. It generated a laser sheet at a nominal depth of $4D$ beneath the free surface. Images were recorded by a high-resolution CCD camera located beneath the wave tank. A mirror located immediately beneath the wave tank reflected patterns of particle images to the CCD camera. This camera had an array of 1000 pixels $\times$ 1016 pixels. Patterns of instantaneous velocity were determined using a frame-to-frame correlation technique. For this arrangement, the effective field of view of the plane of the laser sheet was 87.9 mm $\times$ 89.3 mm. The effective window size during interrogation was 32 pixels $\times$ 32 pixels, with an overlap of 50%. The effective grid size of the pattern of velocity vectors was 1.42 mm. An exceptional case is for imaging of the phase-locked patterns at $KC = 12$; the effective field of view was 58.9 mm $\times$ 59.9 mm, with an effective grid size of 0.95 mm of the pattern of velocity vectors.

A high-sensitivity strain gauge system, which is designated in the top schematics of figure 1(*a*), provided the instantaneous moments due to the in-line (x) and transverse (y) forces acting on the cylinder. The centre of the strain gauge system was at an elevation of 210 mm, which corresponded to $16.5D$ above the quiescent free surface. The outputs from the strain gauge signal conditioners/amplifiers were fed to the analog-to-digital board of the laboratory microcomputer. The in-line and transverse forces generated moments, which were normalized by $(1/2)\rho U_0^2 D L^2$, to give the in-line moment coefficient C_x^* and transverse moment coefficient C_y^*. In this term for normalization, U_0 represents the amplitude of the horizontal velocity fluctuation of the wave motion at the free surface, and D and L are the diameter and submerged length of the cylinder.

3. Quasi-two-dimensional (sectional) flow patterns

Figures 2 to 10 show patterns of the sectional flow structure for values of the Keulegan-Carpenter $KC = 7$, 12, and 18, which generate three generic regimes of vortex shedding. Since the local KC varies along the span of the cylinder, sectional patterns at different spanwise locations differ. For the present investigation, all the sectional patterns were obtained at a fixed spanwise location near the free surface, which was illuminated by the horizontal laser sheet (plan view), as indicated in figures 1(*a*) and 1(*b*). For each phase–averaged representation, four instantaneous images were employed. The aim of this averaging process was to yield smoothing of the instantaneous images, rather than to obtain a convergent phase average; clearly, a larger number of instantaneous images is required for a true phase average, and they could not be readily acquired using the present experimental approach.

At the lowest value of $KC = 7$, the patterns of figure 2 show the possible modes of vortex formation in terms of patterns of instantaneous and averaged velocity vectors $\boldsymbol{V}$ and $\langle \boldsymbol{V} \rangle$, as well as corresponding patterns of vorticity ω_z and $\langle \omega_z \rangle$. All instantaneous images were acquired at the same phase of the wave motion; it corresponded to a phase of the free-surface deflection midway from the crest to the trough of the wave at the location of the cylinder, as illustrated by the wave profile in figure 1(*b*). These instantaneous images are designated as (i), (ii), and (iii) in figure 2. For the set of images designated as (i), the pattern of $\boldsymbol{V}$ shows a rightward directed jet immediately adjacent to the surface of the cylinder and a leftward jet at a location well away from the surface of the cylinder. The pattern of ω_z shows an inclined elongated region of negative ω_z formed from the right-hand surface of the cylinder, as well as a cluster of positive (thick lines) ω_z apparently formed during the previous half-cycle. Another positive concentration is located adjacent to the surface of the

https://doi.org/10.1017/S0022112004001612 Published online by Cambridge University Press

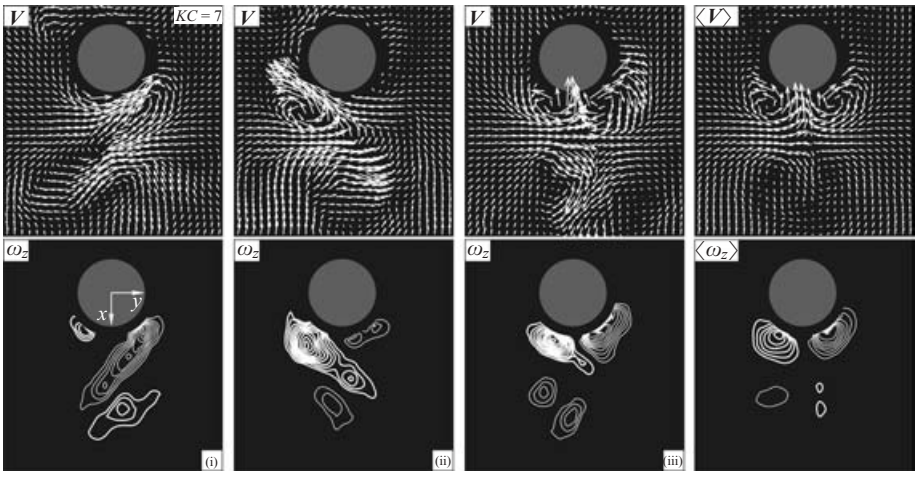


FIGURE 2. Patterns of instantaneous and phase-averaged velocity and vorticity for a value of Keulegan-Carpenter number $KC = 7$. Minimum and incremental values of vorticity contours are $\omega_{min} = \pm 6\,\mathrm{s}^{-1}$ and $\Delta\omega = 3\,\mathrm{s}^{-1}$.

cylinder, which represents the initial stage of process of the large-scale elongated structure.

The set of images (ii) shows, in essence, a mirror image of the patterns of (i) with respect to the x-axis. Both types of patterns (i) and (ii) are therefore admissible instantaneous states of the flow structure and, in addition to these states, a symmetrical mode represented by the set of images (iii) may also occur. The variety of these sectional patterns is due to the three-dimensional behaviour of the flow structure along the span of the cylinder, which will be further addressed, in conjunction with spanwise flow patterns in the following section. In an investigation focusing on a lower range of KC, Ozgoren & Rockwell (2004) observed conceptually similar, but less pronounced, patterns of vorticity ω_z at $KC = 6.16$; they did not address, however, the corresponding patterns of $\boldsymbol{V}$ and the phase averages of ω_z and $\boldsymbol{V}$.

Each of the images (i) to (iii) occurs at essentially the same phase of the wave cycle, so it is appropriate to consider their phase averages $\langle \boldsymbol{V} \rangle$ and $\langle \omega_z \rangle$, as indicated in the right-hand column of figure 2. The consequence is a symmetrical pattern of vortex formation, whereby the peak levels of vorticity are reduced substantially relative to the values given in the instantaneous images.

At higher values of Keulegan-Carpenter number, $KC = 12$, large-scale clusters of vorticity are formed, as shown in figure 3. The vortices formed are essentially phase locked to the wave motion. The instantaneous horizontal component U of the water particle velocity in the wave is determined at an undisturbed location $2.5D$ to the left of the centre of the cylinder (outside of the field of view shown here). The time history of this velocity component U is shown within the boundary of the cylinder and, furthermore, its vector amplitude is indicated at the left of each image. Since only phase-locked patterns of vortex formation with respect to the wave motion are considered in this series, it is appropriate to show patterns of phase-averaged vorticity $\langle \omega_z \rangle$.

In the image $N = 1$, a large-scale cluster A has been formed, as well as smaller-scale clusters B and A′, adjacent to the surface of the cylinder. In images $N = 2$ and 3, cluster A moves toward the centre of the cylinder, while clusters B and A

https://doi.org/10.1017/S0022112004001612 Published online by Cambridge University Press

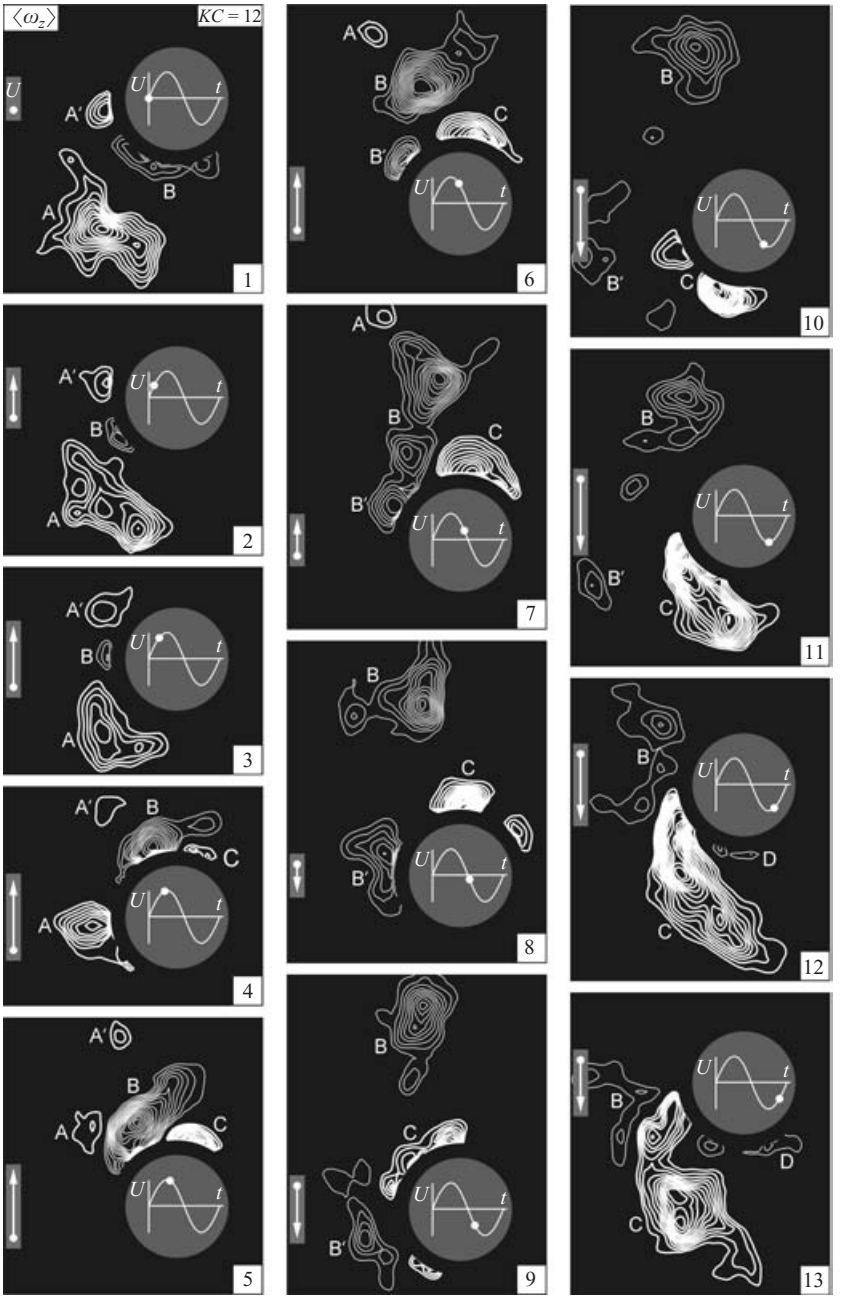


FIGURE 3. Patterns of phase-averaged positive (thick white line) and negative (thin line) vorticity for one cycle of wave motion (labelled $N = 1$–13) at a value of Keulegan-Carpenter number $KC = 12$. Minimum and incremental values of vorticity are $\omega_{min} = \pm 10\,\mathrm{s}^{-1}$ and $\Delta\omega = 5\,\mathrm{s}^{-1}$.

migrate in the clockwise direction about the surface of the cylinder, all in accord with the direction of the wave motion. In images $N = 4$ and 5, cluster A interacts with the surface of the cylinder and, apparently due to three-dimensional effects, experiences substantial attenuation of peak vorticity and circulation. Meanwhile,

https://doi.org/10.1017/S0022112004001612 Published online by Cambridge University Press

cluster B accumulates vorticity until, as indicated in image $N=6$, it appears as a distinct shed cluster of vorticity. In the meantime, positive and negative clusters of vorticity have formed immediately adjacent to the surface of the cylinder; they are designated as C and B′. At a later instant $N=7$, B and B′ are temporarily joined, apparently due to the continued shedding of negative vorticity into B′.

In subsequent images, extending from $N=8$ to 13, the cycle of vortex formation is completed by the large-scale cluster B moving towards and interacting with the cylinder, while experiencing a substantial decrease of peak vorticity. In the meantime, cluster C rotates about the surface of the cylinder in the counterclockwise direction, then departs from the surface.

The entire sequence of images of figure 3 shows large-scale vortex shedding during each half-wave cycle, and the shed vortices tend to form a transverse vortex street in accord with the direction of the wave motion. This pattern of phase-locked vortex formation is remarkably similar to that deduced on the basis of qualitative visualization by Williamson (1985) and Kaye (1989), for planar and wave motions respectively.

Further features of this phase-locked pattern of vortex formation are represented in figure 4, which shows phase-averaged velocity $\langle \boldsymbol{V} \rangle$, vorticity $\langle \omega_z \rangle$ and streamline topology $\langle \psi \rangle$, as well as instantaneous vorticity ω_z. Patterns of $\langle \boldsymbol{V} \rangle$ are shown in the laboratory reference frame, while the patterns of time-averaged streamlines $\langle \psi \rangle$ are in a reference frame moving at the average velocity over the original field of view, as described in § 2. Regarding the patterns of $\langle \boldsymbol{V} \rangle$, consideration of the images $N=1$ to 13 shows that a well-defined swirl pattern, which is often employed to characterize the presence of a well-defined vortical structure, occurs only in images $N=1$, 7 and 13. Direct comparison with the patterns of $\langle \omega_z \rangle$ reveals that these localized swirls are associated with large-scale clusters of vorticity well removed from the cylinder surface. Other well-defined concentrations of vorticity, having smaller circulation, are located closer to the surface of the cylinder. They are not represented by the patterns of $\langle \boldsymbol{V} \rangle$ with this reference frame. The dimensionless moment coefficients C_x^* and C_y^*, corresponding to the in-line and transverse components respectively, are designated in the inset of image $N=10$. This representation allows interpretation of the images with respect to the phases of these loading coefficients. In addition, examination of the variation of the coefficient C_y^* shows that it behaves similarly to the transverse force generated in planar oscillatory flows (e.g. Williamson 1985), as well as to C_y^* of mode U generated in an intermediate water wave (Yang & Rockwell 2002). The coefficient C_x^*, however, shows an almost sinusoidal profile, which mimics C_x^* of mode S in the intermediate water wave (Yang & Rockwell 2002), but differs from the severely deformed shape of the peak of the in-line force coefficient observed for planar oscillatory flows.

Comparison of the patterns of $\langle \psi \rangle$ of figure 4 indicates that the centres of spiralling streamline patterns (foci) generally occur only at the positions of localized swirls of velocity vectors, i.e. at $N=1$, 7, and 13, an exception being the top of the image at $N=10$, which shows a focus corresponding to the cluster of large-scale negative vorticity $\langle \omega_z \rangle$. That is, even though the reference frame has been shifted substantially for construction of the patterns of $\langle \psi \rangle$, only the largest-scale clusters of vorticity, which are well removed from the surface of the cylinder, are represented by the foci of $\langle \psi \rangle$. This observation is in accord with the results of Justesen (1991) and Iliadis & Anagnostopoulos (1998). Despite the fact that these patterns of vortex formation are, in essence, phase-locked, it is possible to observe variations in the stability of the foci of the patterns of $\langle \psi \rangle$. For example the spiral streamline patterns associated with the

https://doi.org/10.1017/S0022112004001612 Published online by Cambridge University Press

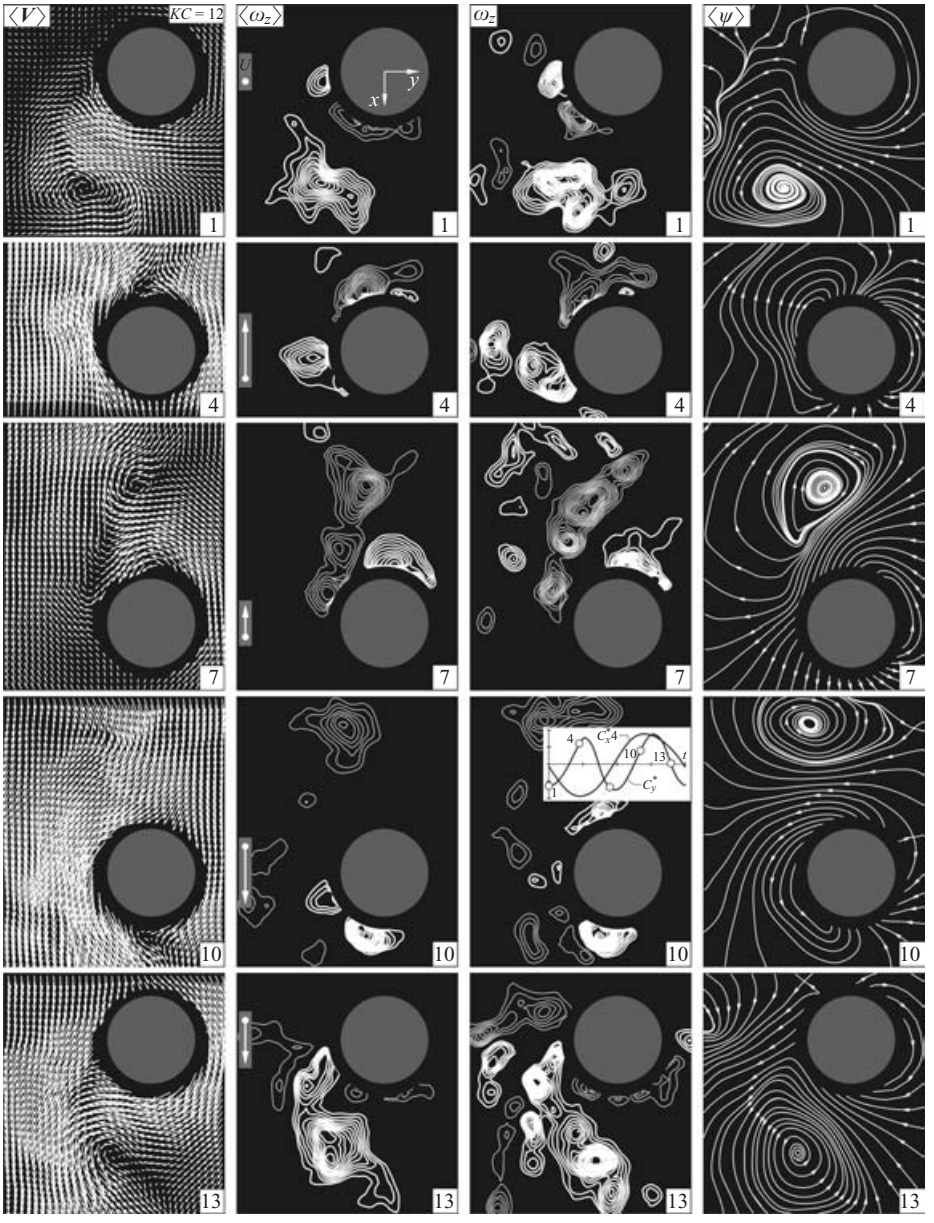


FIGURE 4. Comparison of patterns of velocity, vorticity, and streamlines at selected instants of the wave cycle ($N = 1, 4, 7, 10$ and 13) for a value of Keulegan-Carpenter number $KC = 12$. Patterns of velocity vectors are shown in the laboratory frame, while streamline patterns are in a frame moving at the average velocity of the (original) field of view. Values of minimum and incremental vorticity are $\omega_{min} = \pm 10\,\mathrm{s}^{-1}$ and $\Delta\omega = 5\,\mathrm{s}^{-1}$.

foci in images $N = 1$, 7 and 10 spiral inward towards the focus (centre), and therefore represent stable foci. On the other hand, the pattern of $N = 13$ spirals outward, and therefore represent an unstable focus. Furthermore, the detailed structure of the interior portion of the spiral streamline patterns can exhibit either one or two closed streamlines, i.e. limit cycles, as evident in images $N = 10$ and 7.

https://doi.org/10.1017/S0022112004001612 Published online by Cambridge University Press

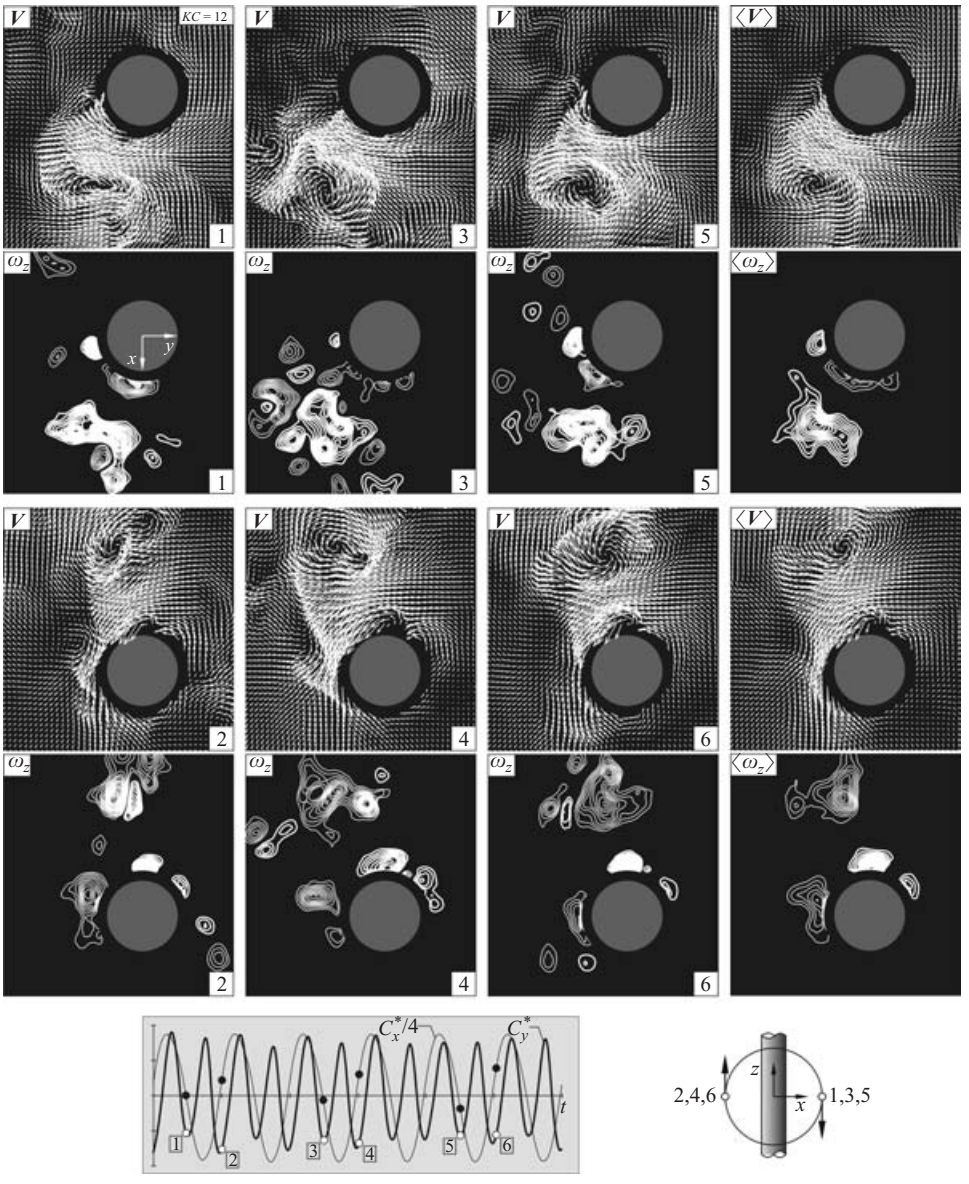


FIGURE 5. Direct comparison of patterns of instantaneous and phase-averaged velocity and vorticity with instantaneous traces of moment coefficients $C_x^*$and C_y^* due to in-line and transverse forces for $N = 1$–6. In this case, C_y^* is phase locked with both C_x^* and the wave motion. Keulegan-Carpenter number $KC = 12$. Patterns of velocity are in the laboratory frame. Minimum and incremental values of vorticity are $\omega_{min} = \pm 10\,\mathrm{s}^{-1}$ and $\Delta\omega = 5\,\mathrm{s}^{-1}$.

Finally, representations of the instantaneous structure of the vortex formation are given by the patterns of ω_z of figure 4. Comparison with the phase-averaged representations $\langle\omega_z\rangle$ indicates that although the overall features of the larger-scale concentrations of vorticity are quite similar, the patterns of ω_z typically show a number of embedded small-scale structures.

Figure 5 shows a comparison of patterns of instantaneous and phase-averaged velocity $\boldsymbol{V}$, $\langle\boldsymbol{V}\rangle$ and vorticity ω_z, $\langle\omega_z\rangle$. The purpose of this comparison is to illustrate

https://doi.org/10.1017/S0022112004001612 Published online by Cambridge University Press

the typical deviations of the instantaneous states of the flow. These images are referenced with respect to the corresponding traces of the in-line $C_x^*/4$ and transverse C_y^* moment coefficients. The instants at which images were acquired are in accord with the local particle trajectory of the wave motion, as shown in the lower right schematic of figure 5. These instants approximately correspond to the maximum negative value of C_y^*. Due to the fact that the period of C_y^* is one-half that of C_x^*, images $N = 1$, 3, and 5 correspond to decreasing C_x^*, while images $N = 2$, 4, and 6 represent increasing C_x^*. It is evident that the patterns of ω_z show a number of small-scale concentrations of positive and negative vorticity that are not evident in the corresponding phase-averaged pattern of $\langle\omega_z\rangle$. These small-scale concentrations have two origins. The first, which is evident within the large-scale clusters of ω_z, arises from a Kelvin–Helmholtz-like instability of the separating shear layer that feeds into the large-scale cluster of vorticity. The second origin of the small-scale concentration is the residual of larger-scale concentrations of vorticity formed during an earlier part of the oscillation cycle(s), which have decayed to relatively low values of circulation.

The duration and frequency of occurrence of phase-locked regions over a relatively large number of wave cycles at $KC = 12$ can be described as follows. For a continuous record of 1000 wave cycles, the duration of regions of phase-locking extended from 3 to 10 wave cycles, i.e. 6 to 20 cycles of the transverse moment coefficient. Approximately 50 of these phase-locked regions occurred over the record of 1000 wave cycles.

The phase-locked patterns of vorticity represented by the images of figure 5 were interrupted by non-phase-locked patterns. The variability of these types of patterns, in relation to the corresponding in-line moment coefficient C_x^* and transverse moment coefficient C_y^*, is shown in figure 6. Inspection of the trace of C_y^* indicates that it is strongly modulated, while the form of the in-line coefficient C_x^* is relatively unaffected. Images $N = 1$, 3, and 5 are acquired at the same phase in every other wave cycle, as illustrated in the lower right schematic, which correspond to approximately the same phase of the trace of C_x^*. At these instants, the value of C_y^* has a local minimum at $N = 1$, and broadly ill-defined maxima at $N = 3$ and 5. The physical origin of these variations is evident in the patterns of instantaneous vorticity ω_z. Images $N = 1$ and 3 show patterns of ω_z that are approximately mirror images of each other, whereas the image of $N = 5$ represents an approximately symmetrical pattern, but with the positive (thick line) vorticity contours having a substantially higher value of peak vorticity than the negative concentration. Due to this variability of patterns of ω_z, the phase-averaged consequence $\langle\omega_z\rangle$ is a nearly symmetrical pattern of very low-level vorticity contours. Generally similar observations hold for the images acquired at $N = 2$, 4, and 6, which are one-half a wave cycle after images at $N = 1$, 3 and 5 respectively. At $N = 2$, the concentration of vorticity formed during the present wave cycle is positive (thick line contours), whereas at $N = 4$, it is negative (thin line contours). The previously formed concentrations of vorticity are, however, located at different streamwise locations. At $N = 6$, the pattern of vortices has a generally similar form as for $N = 2$ but, in addition, the negative (thin line) cluster extends around to the opposite side of the cylinder while retaining substantial levels of vorticity. Again, the consequence of this high variability in states of vortex formation is the tendency to form a symmetrical, very low-level pattern, as indicated in the corresponding averaged image of $\langle\omega_z\rangle$.

At a higher value of Keulegan–Carpenter number, $KC = 18$, the phase-locked patterns of phase-averaged vorticity $\langle\omega_z\rangle$ take the forms shown in figure 7. The format and interpretation of this set of images are the same as for figure 3, representing

https://doi.org/10.1017/S0022112004001612 Published online by Cambridge University Press

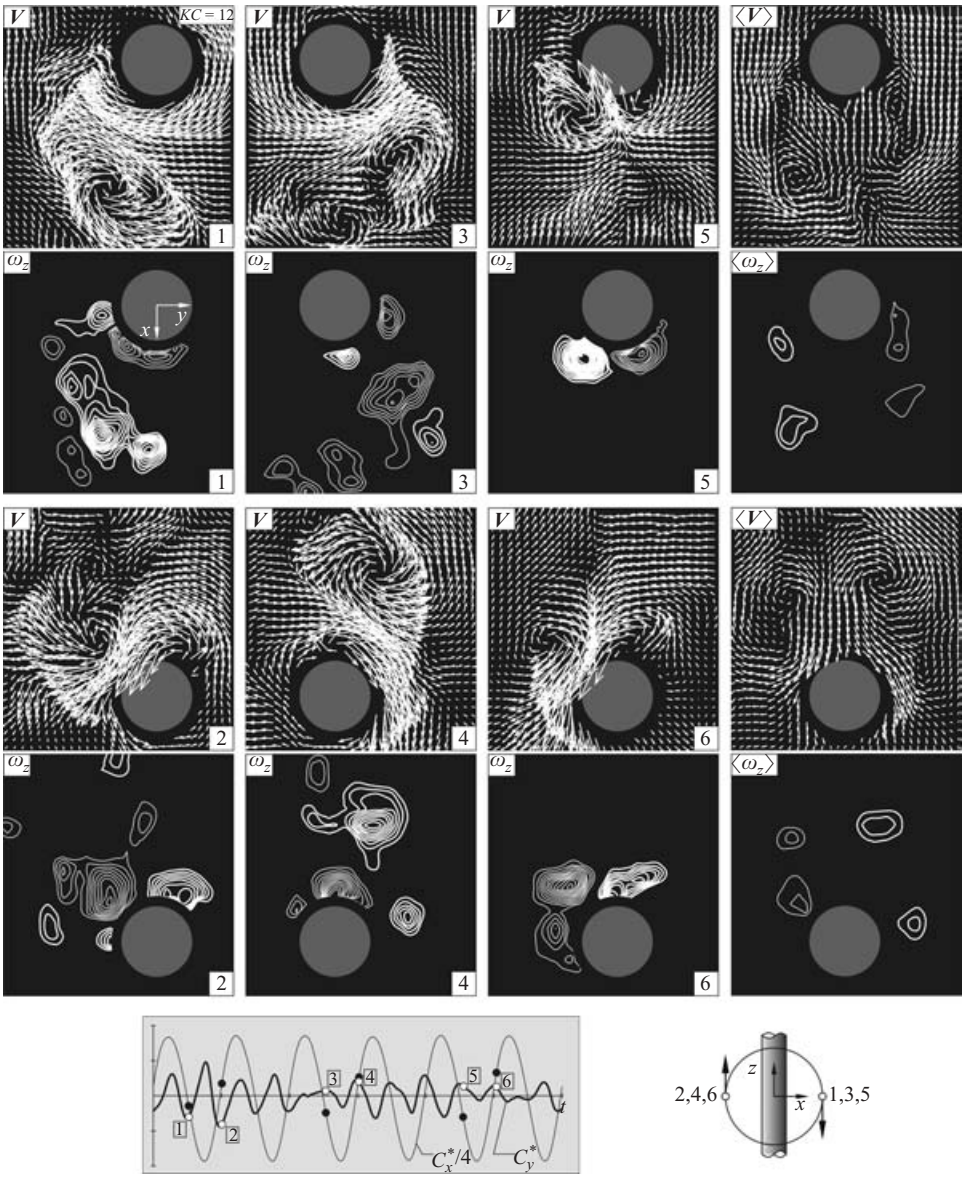


FIGURE 6. Direct comparison of patterns of instantaneous and phase-averaged velocity and vorticity with instantaneous traces of moment coefficients C_x^* and C_y^* due to in-line and transverse forces for $N = 1$–6. For this sequence, C_y^* is phase locked neither with C_x^* nor the wave motion. Keulegan-Carpenter number $KC = 12$. Patterns of velocity are in the laboratory frame. Minimum and incremental values of vorticity are $\omega_{min} = \pm 10\,\mathrm{s}^{-1}$ and $\Delta\omega = 5\,\mathrm{s}^{-1}$.

the lower value of $KC = 12$. The time trace of the horizontal component U of the wave in the undisturbed region of the flow is given within the boundary of each cylinder, and its vector amplitude is drawn at the left of each image. In image $N = 1$, the large-scale cluster A is formed. At $N = 2$, the direction of the wave has reversed and the large-scale cluster moves towards the cylinder, while a previously formed cluster B migrates along the surface of the cylinder in a counterclockwise direction

https://doi.org/10.1017/S0022112004001612 Published online by Cambridge University Press

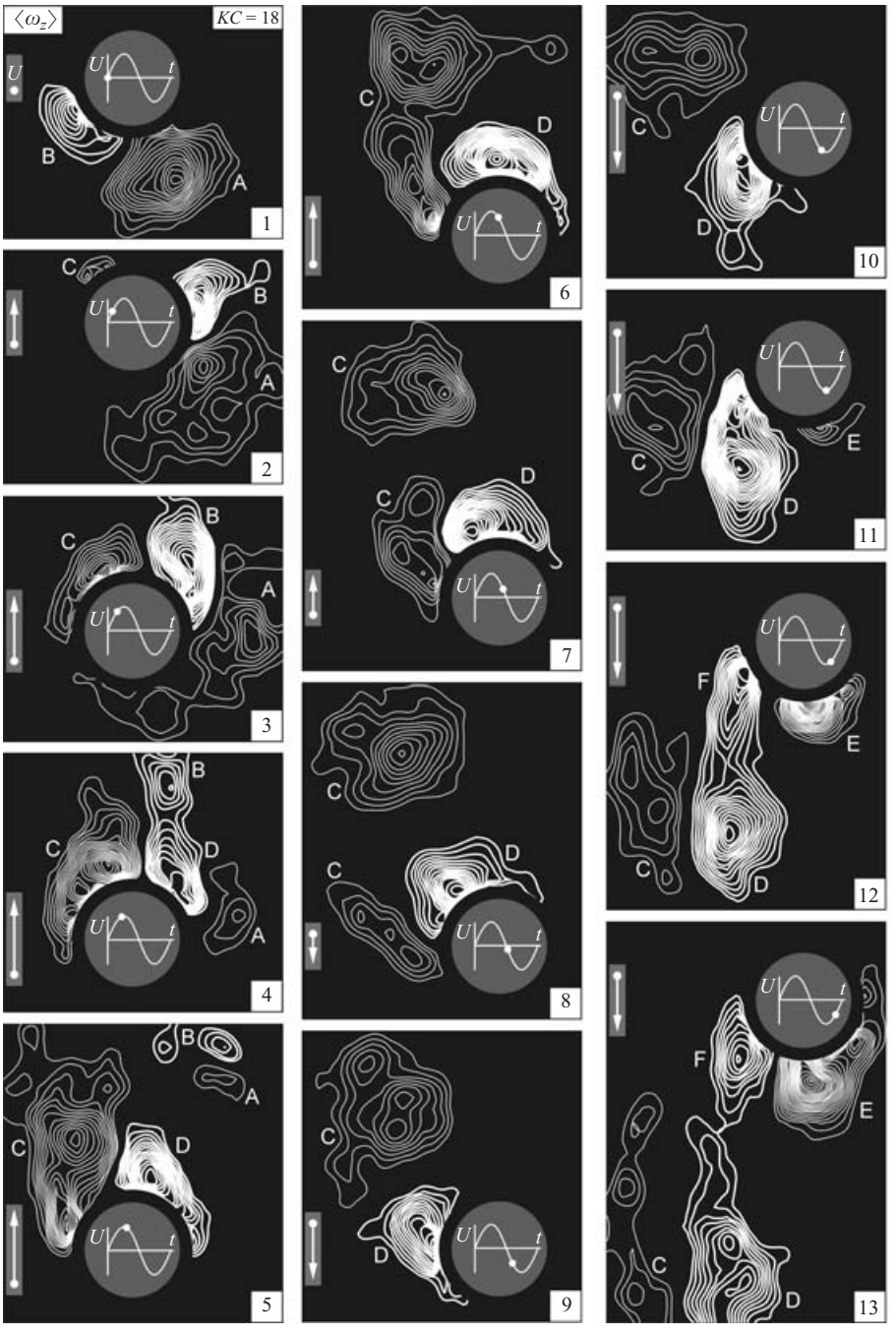


FIGURE 7. Patterns of phase-averaged positive (thick white line) and negative (thin line) vorticity for one cycle of wave motion ($N = 1$–13) at a value of Keulegan-Carpenter number $KC = 18$. Minimum and incremental values of vorticity are $\omega_{min} = \pm 10\,\mathrm{s}^{-1}$ and $\Delta\omega = 5\,\mathrm{s}^{-1}$.

as it continues to develop. At $N = 3$, cluster A is severely distended as it is drawn in opposite directions around the surface of the cylinder, while cluster B continues to develop and cluster C has attained a substantially large value of peak vorticity. At

https://doi.org/10.1017/S0022112004001612 Published online by Cambridge University Press

$N = 4$, the peak vorticity and circulation of A have dramatically decreased. Cluster B has departed from the cylinder, but its successor, D, has rapidly formed and, together with B, forms an elongated cluster. Meantime cluster C continues to grow. At $N = 5$, the residuals of both A and B have paired up and become dramatically smaller, while C and D continue to mature. At $N = 6$ and 7, this process continues, with a portion of C segregating from a cluster immediately adjacent to the cylinder, as indicated in $N = 7$. With the reversal of the wave motion, as indicated in $N = 8$, clusters C and D rotate in a counterclockwise direction about the cylinder, accompanied by a decrease in peak vorticity of C adjacent to the cylinder and preservation of the peak value of C located away from the cylinder. At $N = 9$, the elongated cluster of C evident at $N = 8$ is no longer detectable, whereas the larger-scale cluster C has moved towards the cylinder and, simultaneously, D continues its rotation about the cylinder in the counterclockwise direction. This process continues at $N = 10$ and 11, and at $N = 12$, C and D form a counter-rotating vortex pair, with cluster C having a markedly smaller value of peak vorticity. Furthermore, F, the successor to D, has rapidly formed, and the cluster E adjacent to the surface of the cylinder, which was evident at $N = 11$, has attained a much higher peak value of vorticity. At $N = 13$, clusters F and E continue to develop immediately adjacent to the surface of the cylinder, whereas C and D move well away from the cylinder.

Viewing the aforementioned development of vortex patterns in its entirety, it is generally similar to that represented by the qualitative visualization of Williamson (1985) and Obasaju *et al.* (1988), which involved planar oscillations. In particular, the patterns involving formation of a single counter-rotating vortex pair are fundamentally the same. In comparing with the results of Williamson, whose observations extended over the range $13 \leqslant KC \leqslant 15$, it should be noted that for the present set of images, although $KC = 18$ at the free surface, the local value at the elevation employed for sectional imaging is $KC = 13.9$.

Figure 8 shows excerpts from the sequence of figure 7 in comparison with representative instantaneous patterns of vorticity ω_z, as well as time-averaged patterns of velocity vectors $\langle \boldsymbol{V} \rangle$ and streamlines $\langle \psi \rangle$. Comparing, first of all, the patterns of $\langle \omega_z \rangle$ and ω_z, one sees that the predominant features of the larger-scale clusters of ω_z are replicated in the phase-averaged patterns $\langle \omega_z \rangle$. The swirl patterns of velocity $\langle \boldsymbol{V} \rangle$ indicate the existence of a large-scale cluster of vorticity only in certain instances, typically where a large-scale cluster dominates over a neighbouring cluster. This, however, is not always the case, e.g. the see $\langle \boldsymbol{V} \rangle$ image of $N = 10$. No large-scale vortex is suggested in this laboratory reference frame pattern of $\langle \boldsymbol{V} \rangle$. On the other hand, the streamline $\langle \psi \rangle$ topology constructed in a reference frame corresponding to the average velocity over the original field of view, as discussed in § 2, does show more clearly a larger number of the actual clusters of $\langle \omega_z \rangle$, but this type of representation is still inadequate for identification of coherent vortical structures, such as the positive and negative clusters immediately adjacent to the surface of the cylinder at $N = 7$.

Figure 9 provides three instantaneous states of phase-locked flow patterns, which occurred sequentially over five wave cycles. These states are represented by $\boldsymbol{V}$ and ω_z in comparison with the corresponding phase-averaged patterns of $\langle \boldsymbol{V} \rangle$ and $\langle \omega_z \rangle$. Generally speaking, the instantaneous patterns show the existence of smaller-scale vortical substructures, which, as indicated previously, are associated with the occurrence of a Kelvin–Helmholtz instability during the process of vortex formation. This train of smaller-scale concentrations, which culminates in a larger-scale cluster of vorticity, is particularly evident in the images of ω_z at $N = 2$, 4 and 6.

https://doi.org/10.1017/S0022112004001612 Published online by Cambridge University Press

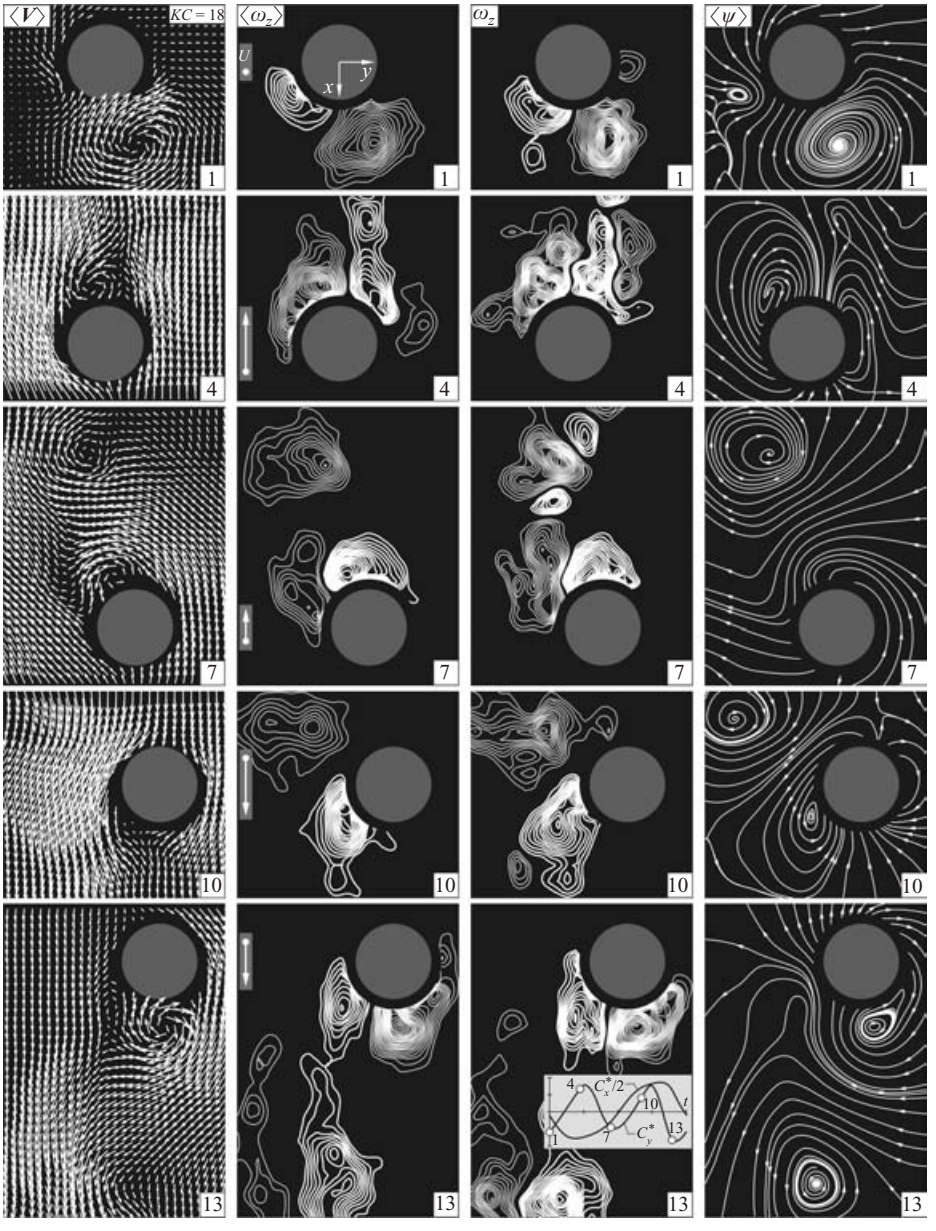


FIGURE 8. Comparison of patterns of velocity, vorticity, and streamlines at selected instants of the wave cycle ($N = 1$, 4, 7, 10 and 13) for a value of Keulegan-Carpenter number $KC = 18$. Patterns of velocity vectors are shown in the laboratory frame, while streamline patterns are in a frame moving at the average velocity of the (original) field of view. Values of minimum and incremental vorticity are $\omega_{min} = \pm 10\,\mathrm{s}^{-1}$ and $\Delta\omega = 5\,\mathrm{s}^{-1}$.

On the other hand, the non-phase-locked patterns of figure 10 are markedly more complex, and the trace of the transverse moment coefficient C_y^* is highly irregular. Furthermore, by examining the instants along the trace C_y^* at which images $N = 1$ to 6 were acquired, it is evident that the values of C_y^* are always very small. Generally speaking, the patterns of ω_z are quite non-repetitive for the series $N = 1$, 3 and 5.

https://doi.org/10.1017/S0022112004001612 Published online by Cambridge University Press

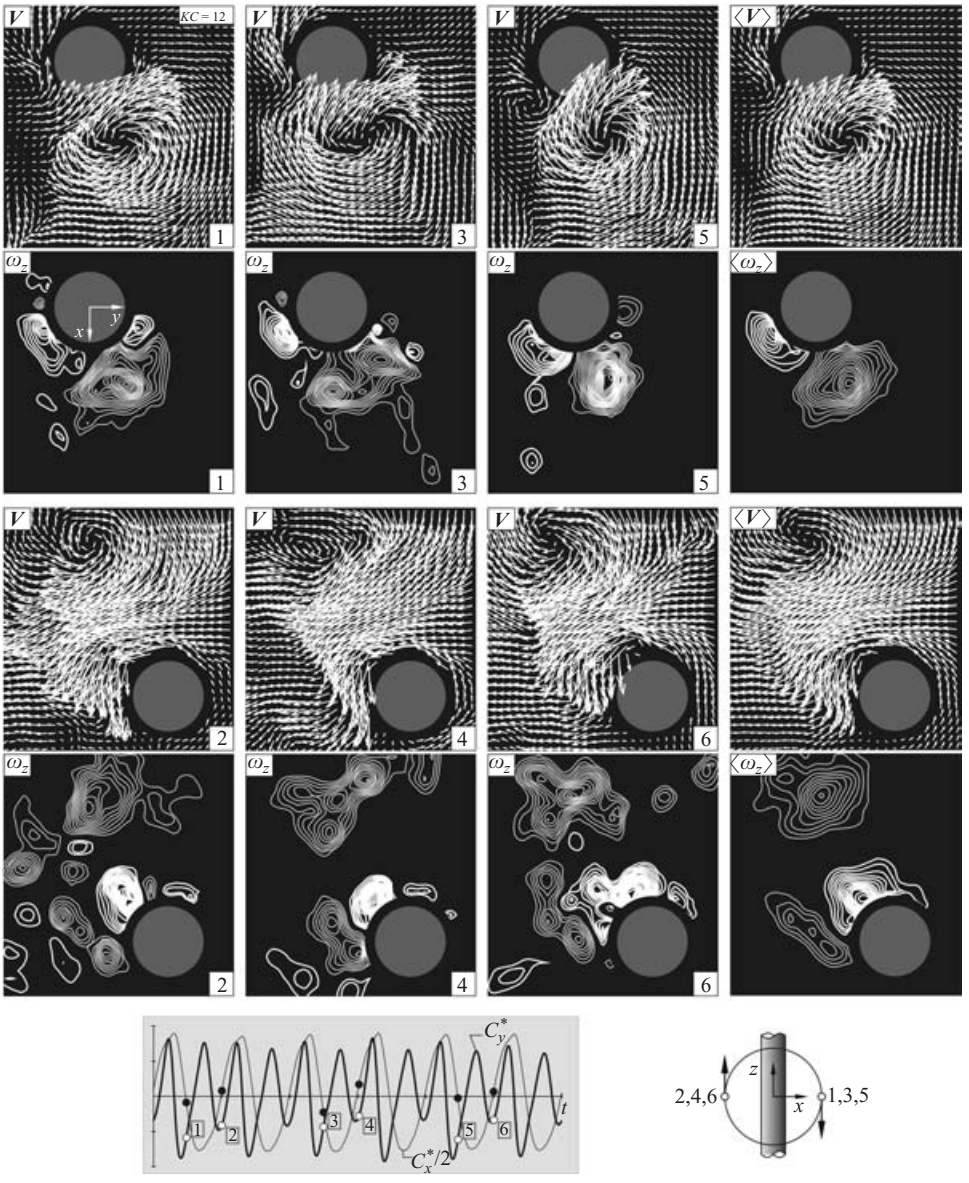


FIGURE 9. Direct comparison of patterns of instantaneous and phase-averaged velocity and vorticity with instantaneous traces of moment coefficients C_x^* and C_y^* due to in-line and transverse forces for $N = 1$–6. In this case, C_y^* is nearly phase locked with both C_x^* and the wave motion. Keulegan-Carpenter number $KC = 18$. Patterns of velocity are in the laboratory frame. Minimum and incremental values of vorticity are $\omega_{min} = \pm 10\,\mathrm{s}^{-1}$ and $\Delta\omega = 5\,\mathrm{s}^{-1}$.

A well-defined pattern of significant vorticity level is, however, evident in the image of $\langle\omega_z\rangle$. For the series $N = 2$, 4 and 6, the patterns at $N = 4$ and 6 are, in a broad sense, nearly mirror images of each other, whereas those at $N = 2$ appear to bear no particular relationship to the others. The phase-averaged consequence in the image of $\langle\omega_z\rangle$ results in very low levels of vorticity.

https://doi.org/10.1017/S0022112004001612 Published online by Cambridge University Press

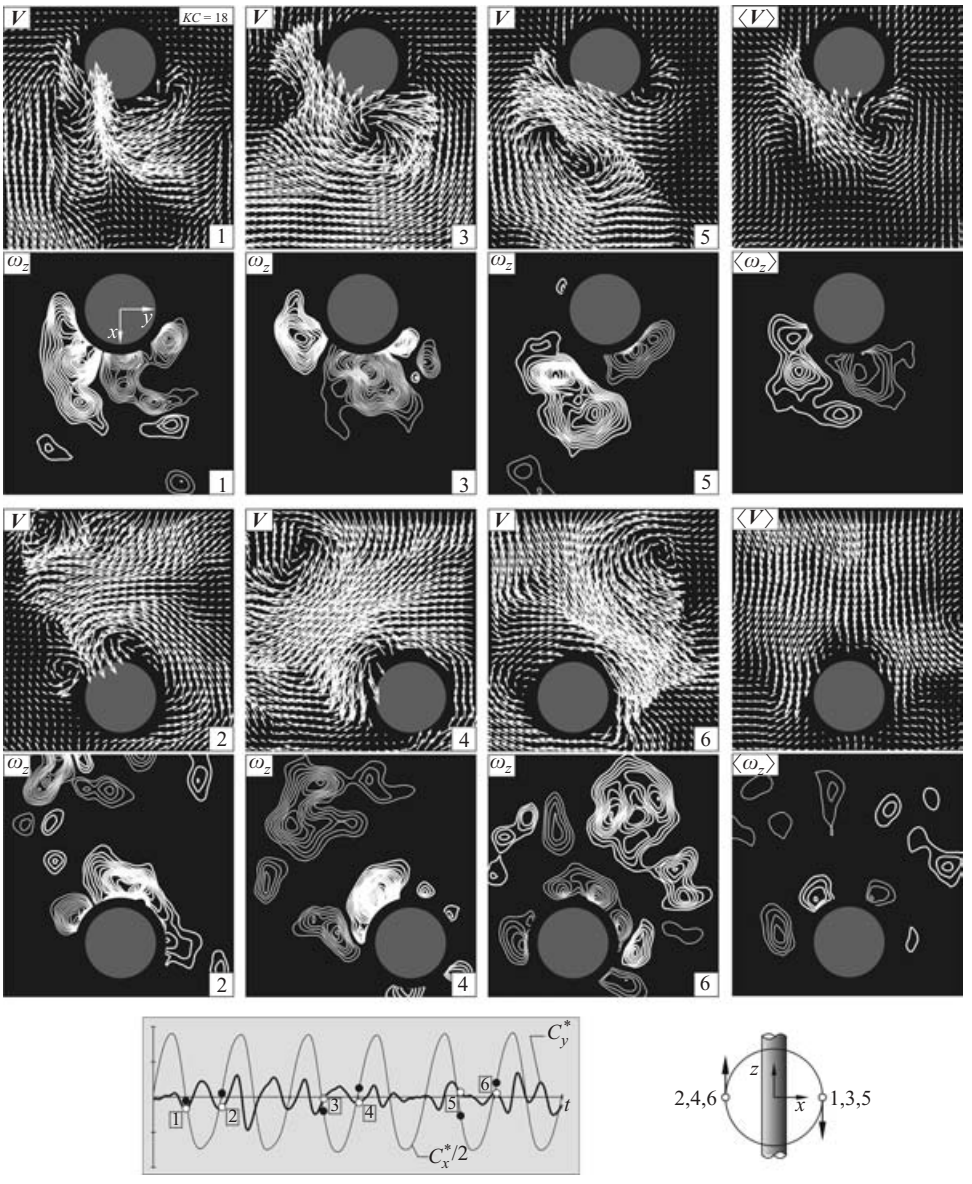


FIGURE 10. Direct comparison of patterns of instantaneous and phase-averaged velocity and vorticity with instantaneous traces of moment coefficients C_x^* and C_y^* due to in-line and transverse forces for $N = 1$–6. For this sequence, C_y^* is phase locked neither with C_x^* nor the wave motion. Keulegan-Carpenter number $KC = 18$. Patterns of velocity are in the laboratory frame. Minimum and incremental values of vorticity are $\omega_{min} = \pm 10\,\mathrm{s}^{-1}$ and $\Delta\omega = 5\,\mathrm{s}^{-1}$.

4. Patterns of three-dimensional flow structure

The patterns of three-dimensional flow structure in the very near wake of the cylinder are given in figures 11 to 13. They were obtained using the orientation of the laser sheet in the (y, z)-plane as indicated in the side and end views of figure 1(a). Further details of this arrangement are described in § 2. In essence, the plane of the laser sheet was located at a distance of $0.5D$ from the surface of the cylinder, where D

https://doi.org/10.1017/S0022112004001612 Published online by Cambridge University Press

is the diameter. Furthermore, the patterns of three-dimensionality were characterized at an instant that corresponded to the onset of pronounced patterns of streamwise vorticity ω_x and cross-stream velocity v. In all images, this instant corresponds to a location midway from the crest to the trough of the wave at the position of the cylinder, as illustrated by the surface wave in figure 1(b). This instant also corresponds to very small values of the moment coefficient C_x^*, which represents the in-line force. As a reference, a scale showing the local values of KC as a function of water depth is embedded in an image of vorticity patterns in each of figures 11 to 13. For each phase-averaged representation, unless otherwise specified, four instantaneous images were employed.

At the lowest value of $KC = 7$, which is represented in figure 11, the patterns of instantaneous cross-stream velocity and streamwise vorticity are shown in (a) and (b). These sets of images show two representative states of the three-dimensionality, and the relationship between these states and the transverse moment coefficient C_y^* is evident in each of the schematics. Compare, first of all, the patterns of v. In figure 11(a), a quasi-two-dimensional region of v extends to a certain depth immediately beneath the free surface. This region dominates the transverse moment coefficient C_y^*. Below this region are well-defined alternating patterns of concentrations of v, which have a nearly constant wavelength along the span of the cylinder. For figure 11(b), however, these concentrations, or cells, extend much closer to the free surface, and the trace of the transverse moment coefficient C_y^* has a substantially lower magnitude. The corresponding patterns of streamwise vorticity ω_x show a more ordered form in the image in figure 11(a).

Phase-averaged representations are shown in figure 11(c, d), with the (c) set corresponding to the average of four images and (d) set to thirty-two images. Comparing these two sets of images, it is evident that the higher the number of instantaneous images for the phase average, the more symmetric and smoother the patterns of $\langle v \rangle$ and $\langle \omega_x \rangle$. This implies that from cycle to cycle of the wave motion, the spanwise patterns of the flow structure, i.e. patterns of $\langle v \rangle$ and $\langle \omega_x \rangle$ show: (i) variations in levels of the concentrations of v and ω_x; and (ii) drift of the spatial positions of these concentrations up and down along the centreline of the cylinder. These effects produce the types of plan view images of figure 2, which represent the sectional vortex shedding. It should be noted that by employing low-level contours in a larger number of instantaneous patterns during the averaging process, it is possible to generate a symmetric phase-averaged pattern in the region of low KC. For the present study, the focus is on the larger-scale structures near the free surface, so these averages are not provided herein.

The issue arises as to the effective spanwise wavelength λ of the concentrations of v and ω_x. For images in figure 11(a), the wavelength of v varies in a small range $\lambda/D = 1.7$ to 2.1. This compares with the value of wavelength based on streamwise vorticity ω_x of $\lambda/D = 1.6$ to 2.0. For the other instantaneous image, in figure 11(b), the patterns of v show values of $\lambda/D = 1.6$ to 2.3 and, for those regions where periodicity is evident, the patterns of ω_x indicate $\lambda/D = 1.5$ to 2.2. Viewing these patterns as a whole, it is evident that the variation of λ/D along the span of the cylinder is directly related to local values of KC. This correlation is in accord with previous experimental and numerical simulations of planar oscillatory flows.

At the larger value of $KC = 12$ shown in figures 12(a) to 12(d), the three-dimensional distortions in the near wake region are severe. Phase-averaged velocity vectors $\langle \boldsymbol{V} \rangle$, cross-stream velocity $\langle v \rangle$ and streamwise vorticity $\langle \omega_x \rangle$, are shown in conjunction with instantaneous cross-stream velocity v and streamwise vorticity ω_x. By examination of

https://doi.org/10.1017/S0022112004001612 Published online by Cambridge University Press

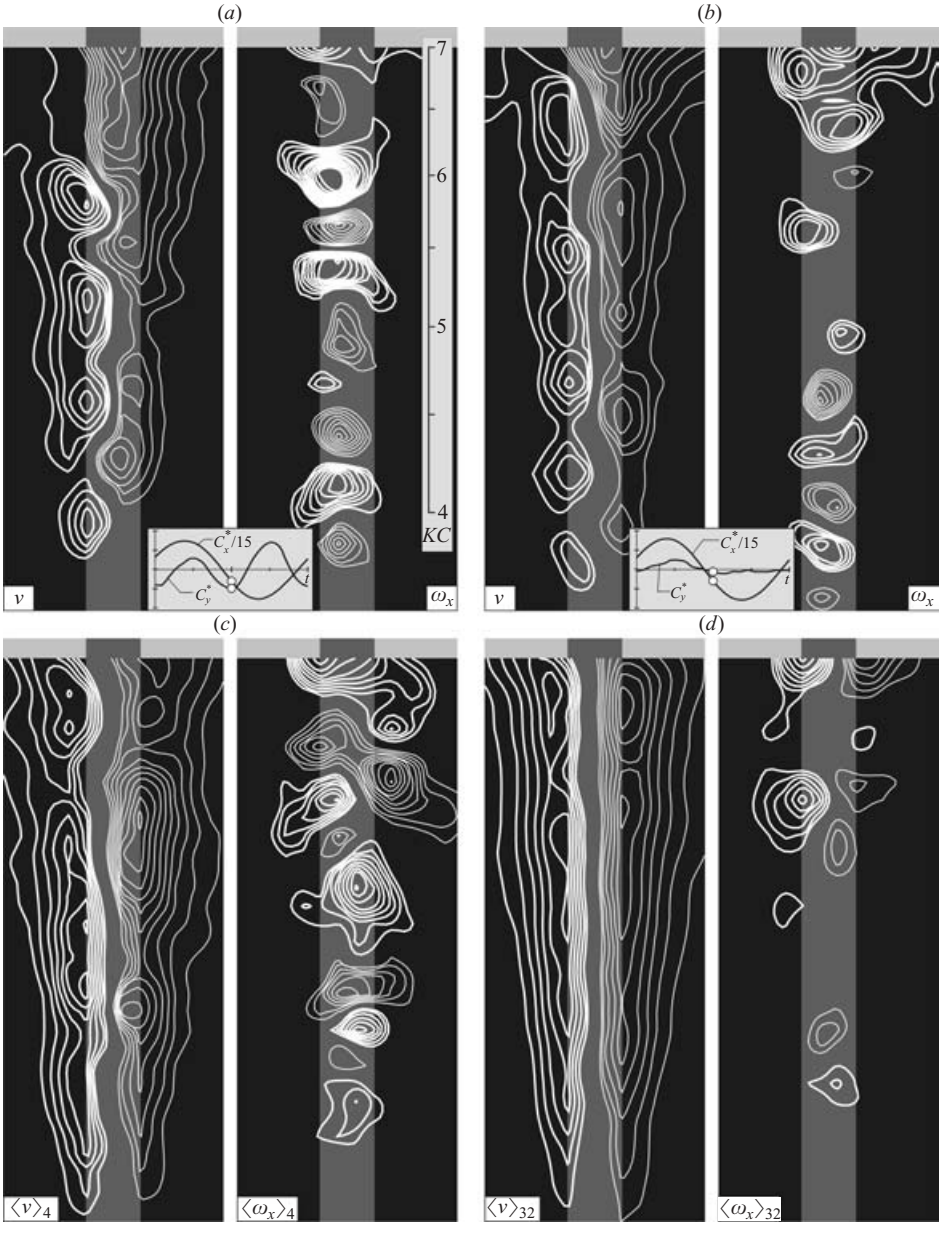


FIGURE 11. Contours of constant transverse (horizontal) velocity component v and streamwise vorticity ω_x. (a, b) Instantaneous patterns in relation to moment coefficients C_x^* and C_y^* due to in-line and transverse forces. (c, d) Phase-averaged representations based on four images and thirty-two images. For contours of instantaneous v, minimum and incremental values are $v_{min} = \pm 7.5\,\mathrm{mm\,s^{-1}}$ and $\Delta v = 2.5\,\mathrm{mm\,s^{-1}}$; for contours of instantaneous ω_x, $\omega_{min} = \pm 0.6\,\mathrm{s^{-1}}$ and $\Delta\omega = 0.2\,\mathrm{s^{-1}}$. For phase-averaged patterns, $v_{min} = \pm\ 6\,\mathrm{mm\,s^{-1}}$ and $\Delta v = 1.5\,\mathrm{mm\,s^{-1}}$; $\omega_{min} = \pm 0.2\,\mathrm{s^{-1}}$ and $\Delta\omega = 0.1\,\mathrm{s^{-1}}$. $KC = 7$.

a large number of images, all taken at the same phase of the wave motion, which corresponds to a nearly zero value of the in-line moment coefficient C_x^*, as indicated in the schematic, it was possible to classify the patterns of the near wake into four

https://doi.org/10.1017/S0022112004001612 Published online by Cambridge University Press

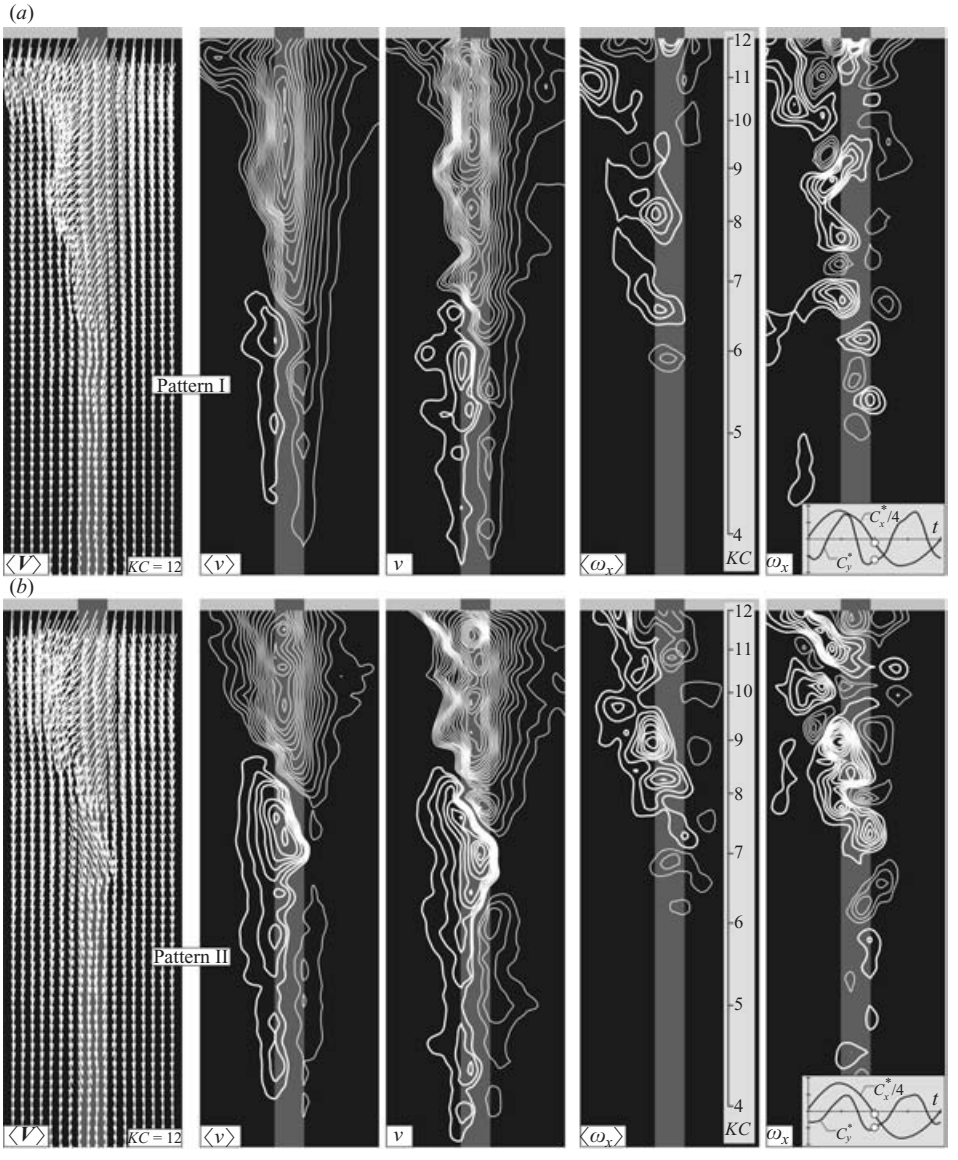


FIGURE 12. For caption see facing page.

forms, designated as patterns *I* to *IV* in figures 12(*a*) to 12(*d*). Pattern *I* represents the case where the transverse velocity component $\langle v \rangle$ is in phase over a relatively large extent from the free surface to a location approximately midway along the span of the cylinder shown in the field of view. At the other extreme, represented by pattern *IV*, this region of constant phase, i.e. constant direction of the component $\langle v \rangle$, is extremely small. Patterns *II* and *III* represent transformations between these extreme states of three-dimensionality. Furthermore, the magnitude of the transverse moment coefficient C_y^* decreases substantially for patterns *I* to *IV*, with nearly undetectable amplitudes for pattern *IV*.

https://doi.org/10.1017/S0022112004001612 Published online by Cambridge University Press

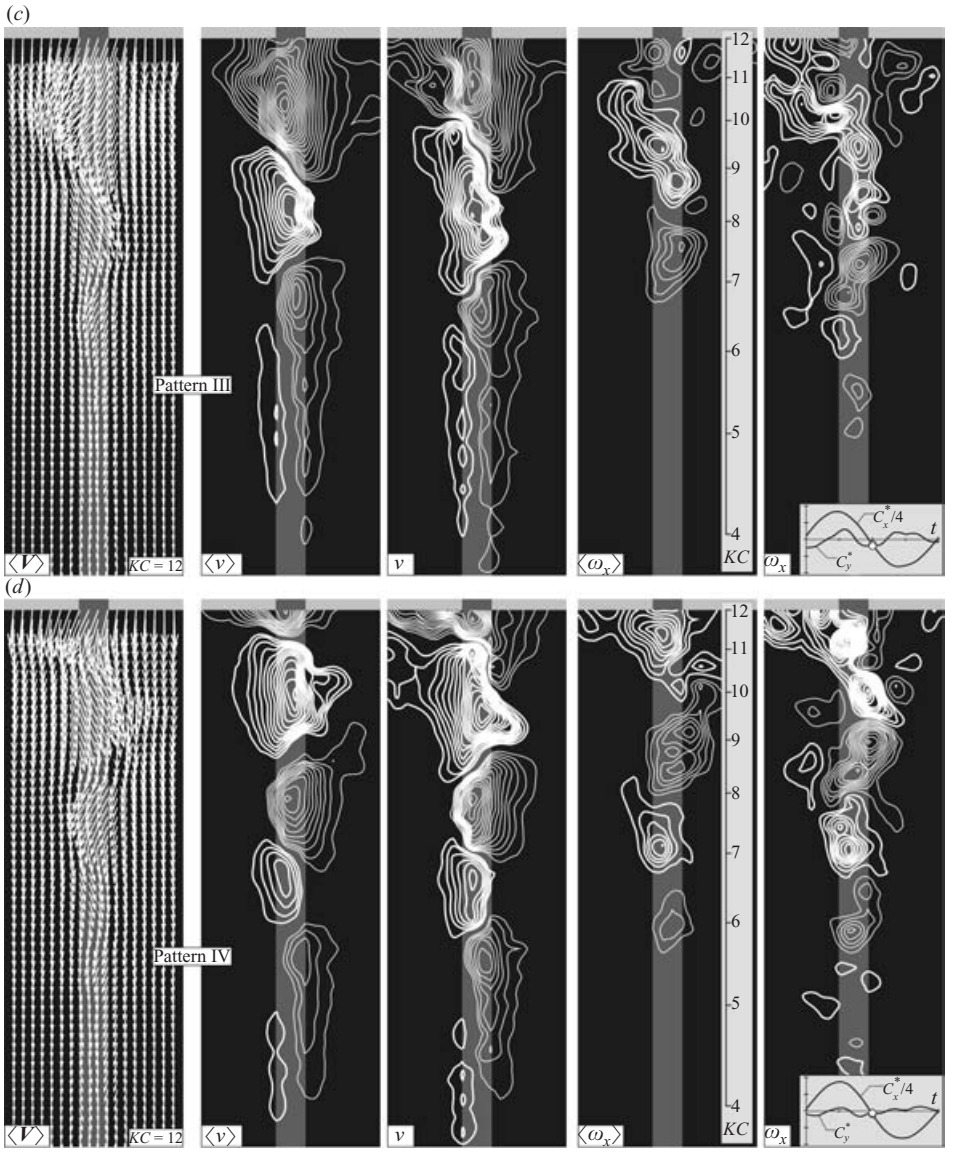


FIGURE 12. Comparison of patterns of velocity vectors $\boldsymbol{V}$, contours of constant transverse (horizontal) velocity v and contours of streamwise vorticity ω_x for patterns (*a*) *I*, (*b*) *II*, (*c*) *III*, and (*d*) *IV*. Instantaneous v and ω_x can be compared with the instantaneous moment coefficients C_x^* and C_y^* due to the in-line and transverse forces. $KC = 12$. Minimum and incremental values of v are $v_{min} = \pm 10\,\mathrm{mm\,s^{-1}}$ and $\Delta v = 5\,\mathrm{mm\,s^{-1}}$. For ω_x, $\omega_{min} = \pm 1\,\mathrm{s^{-1}}$ and $\Delta\omega = 1\,\mathrm{s^{-1}}$.

Consider, first of all, the various representations of pattern *I* of figure 12(*a*), which corresponds to phase-locked quasi-two-dimensional vortex formation, as described in figures 3 to 5. The velocity vectors $\langle \boldsymbol{V} \rangle$ of figure 12(*a*) are predominantly in the downward direction, due to downward movement of the free surface of the wave. Moreover, they are, at least over the top half of the image, inclined to the left, which corresponds to a negative value of cross-stream velocity $\langle v \rangle$. This pattern is evident

https://doi.org/10.1017/S0022112004001612 Published online by Cambridge University Press

in the contours of constant $\langle v \rangle$ over the upper half of the image. On the other hand, over the lower half of the image, the velocity vectors on either side of the cylinder are inclined towards the cylinder centreline, giving patterns of positive (thick line) and negative (thin line) $\langle v \rangle$. This lower half of the field of view corresponds to values of KC extending approximately from 6.5 to 4, and in this region of KC, the vortex formation process is, in its very initial stages, associated with alternating positive and negative small-scale cells having short spanwise wavelength. This pattern contrasts with the one-sided large-scale vortex formation that occurs at higher values of KC as one approaches the free surface. The representative pattern of instantaneous v shows a remarkably similar form to the phase averaged $\langle v \rangle$. The patterns of phase-averaged streamwise vorticity $\langle \omega_x \rangle$, in figure 12(a), are dominated by positive (thick line) $\langle \omega_x \rangle$. The corresponding instantaneous image shows these positive clusters at roughly the same spanwise location, but smaller-scale negative concentrations are generally interspersed between them.

The features of pattern *II* are given in figure 12(b). In this case, the spanwise extent of the contours of negative $\langle v \rangle$ and v is substantially reduced relative to that of pattern *I*. At the lower edge of this pattern, positive clusters of $\langle v \rangle$ and v start to develop and gradually become dominant along the span. At sufficiently large depth beneath the free surface, both positive and negative contours exist side by side. The corresponding patterns of phase-averaged vorticity $\langle \omega_x \rangle$ and instantaneous vorticity ω_x are not well organized, and it is difficult to deduce an effective spanwise wavelength λ/D.

In pattern *III,* shown in figure 12c, the phase-averaged velocity vectors $\langle \boldsymbol{V} \rangle$ show a wavy-like form, whose amplitude decreases with increasing depth beneath the free surface. The consequences of this waviness are the patterns of $\langle v \rangle$ and v, which show alternating large-scale clusters of $\langle v \rangle$ along the span. Moreover, the depthwise extent of the uppermost set of contours of negative $\langle v \rangle$ is significantly smaller than that of pattern *II*. The patterns of phase-averaged $\langle \omega_x \rangle$ and instantaneous ω_x vorticity are relatively unorganized. If one considers, however, the pattern of $\langle \omega_x \rangle$, it is evident that the peak values occur at the zero crossings of the corresponding pattern of $\langle v \rangle$, and, according to these patterns, $\lambda/D = 6.5$.

The extreme pattern *IV*, in figure 12(d), shows a larger number of smaller-scale clusters of $\langle v \rangle$ and v along the span of the cylinder and, furthermore, the depthwise extent of the region of negative (thin line) $\langle v \rangle$ and v immediately beneath the free-surface has decreased dramatically relative to its extent shown in the images of pattern *III*. The patterns of streamwise vorticity $\langle \omega_x \rangle$ and ω_x now show a more ordered form. Again, their extrema occur at the zero crossings of the patterns of $\langle v \rangle$ and v. The spanwise wavelength of the patterns of all of the aforementioned patterns is approximately $\lambda/D = 6.5$.

For the highest value of $KC = 18$, the layout and format of patterns *I* to *IV*, which are shown in figures 13(a) to 13(d), is the same as that for figures 12(a) to 12(d). Whereas the patterns of *I* to *IV* for figures 12(a) to 12(d) allow classification according to the depthwise extent of the negative clusters of $\langle v \rangle$ and v immediately beneath the free surface, such a classification is not possible at this value of $KC = 18$. Patterns *I* to *IV* are, however, generally defined in terms of an increasing number of zero crossings between the positive and negative regions of $\langle v \rangle$ beneath the free surface. Note the switch in sign of $\langle v \rangle$, at an elevation immediately beneath the free surface, of pattern *II* relative to pattern *I*. It is reflected in the sign of the transverse moment coefficient C_y^*, which is essentially inverted for pattern *II* relative to pattern *I*. For patterns *III* and *IV*, the magnitudes of C_y^* averaged over the cycle of wave motion are very small.

https://doi.org/10.1017/S0022112004001612 Published online by Cambridge University Press

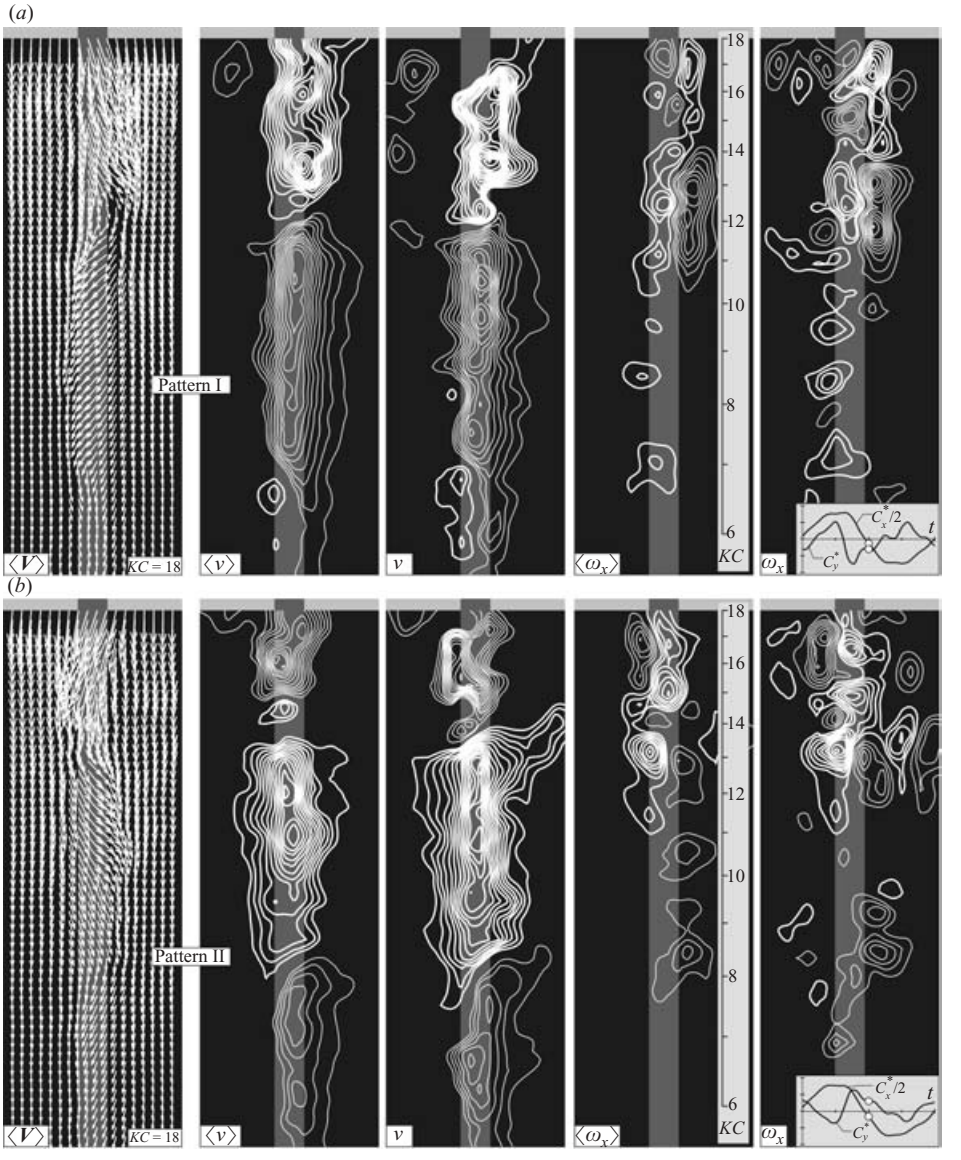


FIGURE 13(*a*, *b*). For caption see next page.

Consider pattern *I* in figure 13(*a*); it is phase-locked with the wave motion, and corresponds to the quasi-two-dimensional vortex formation discussed in figures 7 to 9. Immediately beneath the free surface, contours of positive (thick line) $\langle v \rangle$ and v are evident. Embedded within these larger-scale structures are smaller-scale concentrations having a spanwise wavelength of approximately $\lambda/D = 2.4$. At a larger depth beneath the free surface, negative (thin line) contours of $\langle v \rangle$ and v extend over a substantial spanwise extent.

In pattern *II* of figure 13(*b*), the images show negative contours of v and $\langle v \rangle$ immediately beneath the free surface, in comparison with the positive contours of pattern *I*. Hence the inversion of the peak of C_y^* occurs, as indicated in the insets of

https://doi.org/10.1017/S0022112004001612 Published online by Cambridge University Press

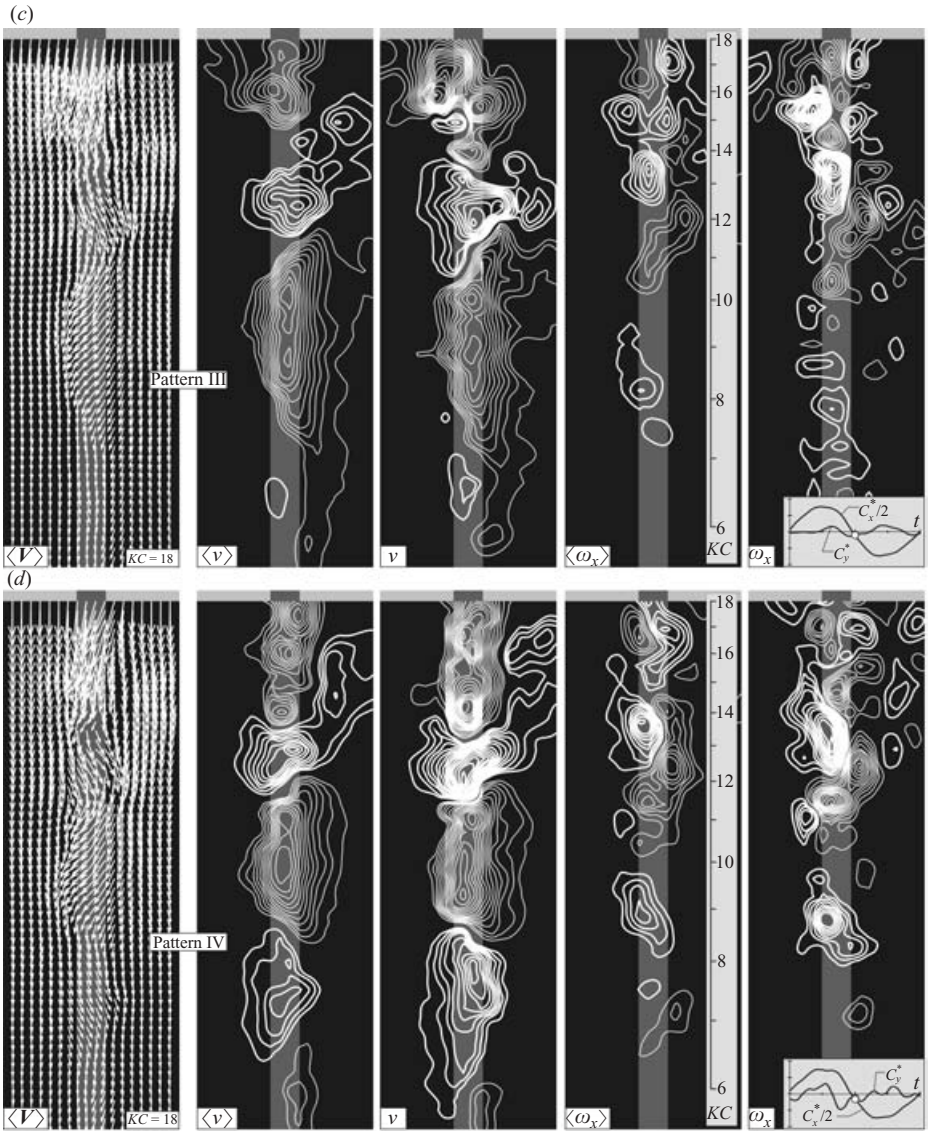


FIGURE 13. Comparison of patterns of velocity vectors $\boldsymbol{V}$, contours of constant transverse (horizontal) velocity v and contours of streamwise vorticity ω_x for patterns (*a*) *I*, (*b*) *II*, (*c*) *III*, and (*d*) *IV*. Instantaneous v and ω_x can be compared with the instantaneous moment coefficients C_x^* and C_y^* due to the in-line and transverse forces. $KC = 18$. Minimum and incremental values of v are $v_{min} = \pm 15\,\mathrm{mm\,s}$ and $\Delta v = 7.5\,\mathrm{mm\,s}$. For ω_x, $\omega_{min} = \pm 2\,\mathrm{s}^{-1}$ and $\Delta\omega = 2\,\mathrm{s}^{-1}$.

patterns *I* and *II*. In pattern *III* (figure 13*c*), contours of $\langle v \rangle$ and v show a smaller spanwise extent involving three well-defined clusters of $\langle v \rangle$ and v along the span.

Finally, in pattern *IV* of figure 13 (*d*), the number of detectable clusters along the span includes a total of four regions of negative and positive $\langle v \rangle$ and v. The contours of constant $\langle \omega_x \rangle$ and ω_x now take on a more ordered form, yet it is difficult to determine an effective spanwise wavelength λ/D in view of the fact that these clusters of vorticity show an interlaced pattern along the span of the cylinder.

https://doi.org/10.1017/S0022112004001612 Published online by Cambridge University Press

Taken together, the images representing patterns *I* to *IV* suggest that when a larger number of zero crossings occur over the upper half of the cylinder displayed in each layout, the magnitude of the transverse moment coefficient C_y^* is decreased. For example, in the images corresponding to patterns *I* and *II*, the number of zero crossings of $\langle v \rangle$ over the upper half of the cylinder is only one. On the other hand, for patterns *III* and *IV*, two zero crossings occur, and the magnitude of C_y^* decreases substantially. A reason for this observation is that the velocity amplitudes of the wave are largest in the region near the free surface, therefore the contribution to the transverse moment coefficient C_y^* is also the largest in this region.

5. Concluding remarks

Interaction of a deep-water wave with a vertical cylinder can give rise to patterns of both phase-locked and non-phase-locked quasi-two-dimensional and three-dimensional patterns. Irrespective of whether the quasi-two-dimensional or three-dimensional structure is considered, there is a high correlation between patterns of phase-locked flow structure and high values of transverse loading (moment) coefficient. The in-line loading (moment) coefficient is, however, relatively unaffected. Furthermore, even when patterns of flow structure are not phase locked to the wave motion, the individual non-repetitive patterns of vortex formation, which comprise the non-locked states, are clearly identifiable and can be categorized into basic forms.

5.1. *Quasi-two-dimensional patterns of vortex formation*

At a low value of Keulegan–Carpenter number, $KC = 7$, phase-locked patterns of vortex formation are not attainable in the deep-water wave. Mode inversion, whereby the initially formed locally quasi-two-dimensional vortex occurs from the opposite side of the cylinder, even though the phase of the wave motion is the same, is an inherent feature. This mode inversion, along with the occurrence of a symmetrical mode of vortex formation, yields phase-averaged patterns of quasi-two-dimensional vortex formation that are symmetrical, and thereby not representative of the actual physics of the instantaneous states of the flow.

At the sufficiently high values of $KC = 12$ and 18, phase-locked patterns of locally two-dimensional vortex formation are attainable, and in this case, the magnitude of the transverse loading coefficient C_y^* is relatively large. The quasi-two-dimensional patterns of vortex formation are in general accord with previous observations for planar oscillatory flows, as well as actual wave flows cited in the Introduction. Such visualization, and even patterns of phase-averaged instantaneous streamlines in the wave reference frame, do not show a number of features of the actual patterns of vorticity: (i) elongated layers of vorticity that lead to the formation of large-scale clusters away from the cylinder; (ii) pronounced vorticity concentrations immediately adjacent to the surface of the cylinder; and (iii) small-scale vorticity concentrations within the elongated layer from the surface of the cylinder.

The foregoing features of the vorticity layers associated with vortex formation are evident for both phase-locked and non-phase-locked vortex formation. Phase-locked locally two-dimensional vortex formation from a vertical cylinder in a deep-water wave does not persist for a large number of cycles of the wave motion. Rather, it is interrupted by non-phase-locked vortex formation, which can be categorized into basic patterns of vortices.

https://doi.org/10.1017/S0022112004001612 Published online by Cambridge University Press

5.2. *Three-dimensional flow structure*

Along the span of the cylinder, patterns of total velocity $\boldsymbol{V}$, transverse velocity v, and streamwise vorticity ω_x all provide definitions of basic modes of three-dimensionality. At $KC = 7$, well-defined concentrations of v and ω_x occur along the entire span, and the spacing between local concentrations is directly related to the local value of KC beneath the free surface. In other words, the spanwise wavelength varies in a continuous fashion with increasing depth beneath the free surface, and the local wavelength λ/D is in accord with previous experimental and numerical simulations of planar oscillations, rather than actual wave oscillations.

At larger values of KC, it is possible to identify highly ordered generic patterns of transverse velocity v. Patterns of streamwise vorticity ω_x, which are representative of the local smaller scales of the flow, are embedded within these ordered patterns of v. When the patterns contain unidirectional regions of v that extend over a substantial spanwise extent of the cylinder, especially in the region near the free surface, the magnitude of the transverse loading coefficient C_y^* is relatively large. In general, as the number of zero crossings between positive and negative regions of v increases, the magnitude of C_y^* decreases. In this limit, there is an identifiable relationship with the corresponding patterns of streamwise vorticity ω_x.

Taken together, the patterns of locally two-dimensional and three-dimensional flow structure indicate that non-phase-locked states of locally two-dimensional patterns are associated with a relatively large number of zero crossings of the transverse velocity v along the span of the cylinder. In other words, the existence of locally phase-locked two-dimensional vortex formation is associated with significant regions of spanwise extent of like sign of transverse velocity v.

The authors acknowledge support of the Office of Naval Research under Grants ONR N00014-01-0-0606 and ONR N00014-94-1-0185 monitored by Dr Thomas Swean. Supplemental support was from the National Science Foundation, Grant CTS-9803734, monitored by Dr Michael Plesniak.

REFERENCES

Bearman, P. W., Chaplin, J. R., Graham, J. M. R., Kostense, J. K., Hall, P. F. & Klopman, G. 1985 The loading on a cylinder in post-critical flow beneath periodic and random waves. *Proc. 4th Intl Conf. on Behaviour of Offshore Structures, Delft* (ed. J. A. Battjes), *Developments in Marine Technology*, vol. 2, pp. 213–225. Elsevier.

Bearman, P. W., Graham, J. M. R., Naylor, P. & Obasaju, E. D. 1981 The role of vortices in oscillatory flow about bluff cylinders. *Intl Symp. on Hydrodynamics and Ocean Engng*, pp. 621–644. The Norwegian Institute of Technology.

Chakrabarti, S. K. 1980 In-line forces on a fixed vertical cylinder in waves. *J. Waterway, Port, Coastal and Ocean Div., ASCE* **106**, 134–155.

Dean, R. G., Dalrymple, R. A. & Hudspeth, R. T. 1981 Force coefficients from wave projects I and II. Data including free-surface effects. *Soc. Petrol. Engrs J.* December, 777–786.

Dütsch, H. L. 2000 Numerische simulation mechanischer fluid-struktur-wechselwirkungen bei groβen auslenkungen. PhD Dissertation, University of Erlangen, Nürnberg.

Dütsch, H., Durst, F., Becker, S. & Lienhart, H. 1998*a* Low-Reynolds-number flow around an oscillating circular cylinder at low Keulegan-Carpenter numbers. *J. Fluid Mech.* **360**, 249–271.

Dütsch, H., Durst, F. & Brenner, G. 1998*b* Three-dimensional vorticity structure in the flow around an oscillating circular cylinder at low Reynolds and Keulegan-Carpenter numbers. *Proc. 1998 Conf. on Bluff Body Wakes and Vortex-Induced Vibration* (ed. P. W. Bearman & C. H. K. Williamson). 1998 ASME Fluids Engng Div. (Annual Summer Meeting), Washington, D.C., 21–25 June.

https://doi.org/10.1017/S0022112004001612 Published online by Cambridge University Press

Elston, J. Blackburn, H. M. & Sheridan, J. 2000 The onset of three-dimensionality in the flow generation by an oscillating circular cylinder. Abstract AF1, *53rd Ann. Mtg of Div. Fluid Dynamics, November 19–21, Washington, DC Bull. Am. Phys. Soc.* **45**, 21.

Honji, H. 1981 Streaked flow around an oscillating circular cylinder. *J. Fluid Mech.* **107**, 509–520.

Iliadis, G. & Anagnostopoulos, B. 1998 Numerical visualization of oscillatory flow around a circular cylinder at $Re = 200$ and $KC = 20$ – an aperiodic flow case. *Commun. Numer. Meth. Engng* **14** (3), 181–194.

Ikeda, S. & Yamamoto, Y. 1981 Transverse forces on cylinders in oscillatory flows. *Rep. Dept. Foundation of Engng. and Coastal Engng., Saitama University, Japan*, vol. 10, pp. 1–16.

Iwagaki, Y., Asano, T. & Nagai, F. 1983 Hydrodynamic forces on a circular cylinder placed in wave-current co-existing fields. *Memo Fac. Eng., Kyoto University, Japan* **45**, 11–23.

Justesen, P. 1991 A numerical study of oscillating flow around a circular cylinder. *J. Fluid Mech.* **222**, 157–196.

Kaye, D. 1989 Oscillation of a vertical cylinder in waves. PhD Dissertation, University of Cambridge.

Kozakiewicz, A., Sumer & Fredsøe 1992 Spanwise correlation on a vibrating cylinder near a wall in oscillatory flows. *J. Fluids Struct.* **6**, 371–392.

Lin, J.-C. & Rockwell, D. 1999 Horizontal oscillations of a cylinder beneath a free-surface: vortex formation and loading. *J. Fluid Mech.* **389**, 1–26.

Obasaju, E. D., Bearman, P. W. & Graham, J. M. R. 1988 A study of forces, circulation, vortex modes around a circular cylinder and oscillating flow. *J. Fluid Mech.* **196**, 467–494.

Ozgoren, M. & Rockwell, D. 2004 Interaction of a deep-water wave with a vertical cylinder at low Keulegan-Carpenter number: Transition from phase-locked modes of vortex formation. *Phys. Fluids* **16**, 2700–2703.

Ramberg, S. E. & Niedzwecki, J. M. 1979 Some uncertainties and errors in wave force compuations. *Proc. 11th Offshore Technology Conf., Houston, TX*, vol. 3, pp. 2091–210l. Offshore Technology Conf. 6200N, Central Expressway, Dallas, TX.

Sarpkaya, T. 1984 Discussion of 'quasi 2-d forces on a vertical cylinder in waves' (paper No. 17671 by P. K. Stansby *et al.*). *J. Waterway, Port, Coastal Ocean Engng* **110** (1), 120–123.

Sarpkaya, T. 1986 Force on a circular cylinder in viscous oscillatory flow at low Keulegan-Carpenter numbers. *J. Fluid Mech.* **165**, 61–71.

Sarpkaya, T. 2002 Experiments on the stability of sinusoidal flow over a circular cylinder. *J. Fluid Mech.* **457**, 157–180.

Sarpkaya, T. & Isaacson, M. 1981 *Mechanics of Wave Forces on Offshore Structures.* Van Nostrand Reinhold.

Singh, S. 1979 Forces on bodies in oscillatory flow. PhD Thesis, University of London.

Sirisup, S., Karniadakis, G. E., Yang, Y. & Rockwell, D. 2004 Wave-structure interaction: simulation driven by quantitative imaging. *Proc. R. Soc. Lond.* A **460**, 1–27.

Stansby, P. K., Bullock, G. N. & Short, I. 1983 Quasi-two-dimensional forces on a vertical cylinder in waves. *J. Waterway, Port, Coastal Ocean Engng* **109** (1), 128–132.

Sumer, B. M. & Fredsøe, J. 1997 *Hydrodynamics Around Cylindrical Structures. World Scientific.*

Tatsuno, M. & Bearman, P. W. 1990 A visual study of the flow around an oscillating circular cylinder at low Keulegan-Carpenter numbers and low Stokes numbers. *J. Fluid Mech.* **211**, 157–182.

Tørum, A. 1989 Wave forces on pile in surface zone. *J. Waterway, Port, Coastal Ocean Engng* **115** (4), 547–565.

Williamson, C. H. K. 1985 Sinusoidal flow relative to circular cylinder. *J. Fluid Mech.* **155**, 141–174.

Yang, Y. & Rockwell, D. 2002 Wave interaction with a vertical cylinder: spanwise flow patterns and loading. *J. Fluid Mech.* **460**, 93–129.

https://doi.org/10.1017/S0022112004001612 Published online by Cambridge University Press